JGR Solid Earth

RESEARCH ARTICLE
10.1029/2025JB032558

Special Collection:
Advanced machine learning in solid earth geoscience

Modeling and Inversion for Wave Propagation in Tight Sandstone Reservoirs Using Machine Learning

Fansheng Xiong[1], **Jing Ba**[2], **José M. Carcione**[2,3], **and Zhijian Fang**[2]

[1]Beijing Institute of Mathematical Sciences and Applications, Beijing, China, [2]School of Earth Sciences and Engineering, Hohai University, Nanjing, China, [3]National Institute of Oceanography and Applied Geophysics–OGS, Trieste, Italy

Key Points:

- We propose a machine learning (ML) approach to establish simplified dynamic equations describing wave propagation in sandstone reservoirs
- The new poroelasticity theory is based on a simplification of the Biot-Rayleigh equations
- The local-flow term, which is responsible for wave attenuation, and some elastic constants and other factors are obtained from data and ML

Correspondence to:
J. Ba,
jba@hhu.edu.cn

Citation:
Xiong, F., Ba, J., Carcione, J. M., & Fang, Z. (2026). Modeling and inversion for wave propagation in tight sandstone reservoirs using machine learning. *Journal of Geophysical Research: Solid Earth*, *131*, e2025JB032558. https://doi.org/10.1029/2025JB032558

Received 26 JUL 2025
Accepted 17 DEC 2025

Author Contributions:
Conceptualization: Fansheng Xiong, Jing Ba
Data curation: Zhijian Fang
Formal analysis: Fansheng Xiong, Jing Ba, José M. Carcione
Funding acquisition: Jing Ba
Investigation: Fansheng Xiong, José M. Carcione, Zhijian Fang
Methodology: Fansheng Xiong, Jing Ba, José M. Carcione
Project administration: Jing Ba
Resources: Jing Ba, Zhijian Fang
Software: Fansheng Xiong, Zhijian Fang
Supervision: Jing Ba, José M. Carcione
Validation: Fansheng Xiong, Jing Ba, Zhijian Fang
Visualization: Fansheng Xiong
Writing – original draft: Fansheng Xiong, Jing Ba, Zhijian Fang
Writing – review & editing: Fansheng Xiong, Jing Ba, José M. Carcione

Abstract

Understanding wave propagation in subsurface reservoirs is an important topic in exploration geophysics. Using machine learning (ML), this study aims to develop a hybrid modeling approach that uses data techniques while maintaining the reliability of poroelasticity theory. Simplified dynamic equations for seismic propagation in sandstone reservoirs are established in two steps: Biot-Rayleigh theory is established and then an optimization algorithm in ML is used to identify a simplified equation and calculate a local fluid flow term, which is responsible for wave attenuation, and some of the elastic constants and factors such as the volume ratio of inclusions. The effectiveness of the approach is first tested on synthetic data, and it is shown that almost the same dispersion and attenuation as the original model can be predicted. Data from experimental and borehole measurements are then considered. Examples show that with a few data points the wave velocity can be accurately predicted in different frequency ranges. Although the model has a certain extrapolation capability, the coverage of training data is still required. Finally, the approach is extended to perform porosity inversion. The proposed technique can be extended to reservoirs with different lithologies.

Plain Language Summary

This study combines the theory of poroelasticity with machine learning (ML) to create a general model to describe wave propagation in sandstone reservoirs. The original equation is based on the Biot-Rayleigh theory, and the unknown factors describing the attenuation and elastic properties of a simplified equation are determined with a ML algorithm using a small amount of data. In a purely data-driven approach, all quantitative relationships are unknown and must be learned from the data. In contrast, in the proposed approach, only the unknown factors need to be determined as the framework is built by using the effective poroelasticity theory, which significantly reduces the data set requirements. The established dynamic equations can be successfully matched with experimental data of tight sandstones. In addition, parameter inversion can be performed. The effectiveness of the method is verified with synthetic data and borehole data.

1. Introduction

Wave propagation theories are a powerful tool for predicting and understanding the properties of subsurface rocks. Wave-induced fluid flow occurs and leads to significant dispersion and attenuation of seismic waves (e.g., Borgomano et al., 2019; Carcione et al., 2024; Müller et al., 2010). Improving the model that characterizes this process is crucial for quantitative seismic interpretation as it contains information about the lithology of the reservoir and the fluids in the subsurface.

The modeling of wave propagation is usually based on first principles or (semi-)empirical relationships. Various hypotheses have to be made and complex derivations carried out. However, it is difficult to guarantee that the hypotheses apply in all cases. With the advent of machine learning (ML), many researchers (e.g., Li et al., 2023; Shen et al., 2023; Song et al., 2024; Tsai et al., 2021; Yu & Ma, 2021) have proposed data-driven equation discovery, a ML technique that aims to automatically identify mathematical equations from data sets. Shen et al. (2023) introduced the differentiable programming (DP) approach, which makes the modeling process easier and faster as some complex patterns can be learned from data. It is pointed out that it is unrealistic to rely solely on data to create wave propagation models, as both data quantity and data quality may be insufficient.

In this study, it is proposed to set up dynamic equations in conjunction with data. First, the dynamic equations can be established based on the existing poroelasticity theories. Then, the unknown factors, such as an equation or a model parameter, are set as trainable parameters or determined by neural networks (NNs) from data. Xiong et al. (2021a) used Biot theory (1956, 1962) for shale oil reservoirs, where the elastic constants were learned by

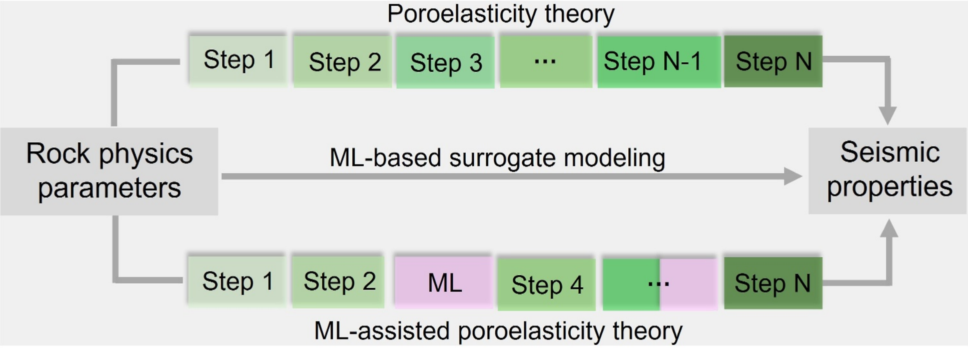

Figure 1. Schematic representation of the approach.

NNs. The attenuation of seismic-band waves was not considered. Similar studies can be found in Xiong & Yong (2022) and Fang et al. (2024).

This study focuses on tight sandstone reservoirs where the geometry of the rocks is complex and generally exhibits heterogeneity (e.g., David & Zimmerman, 2012; Guo et al., 2019; Li et al., 2020; Osorio et al., 2025; Smith et al., 2009; Viswanathan et al., 2022). Theories of double porosity are used to describe the medium and wave propagation. Berryman & Wang (2000) derived dynamic equations but did not consider local flow effects on seismic waves. Later, Pride & Berryman (2003a, 2003b) extended the model to double porosity and double permeability (DPDP) to describe local flows. The DPDP model yields the effective Biot model (EB) assuming that the inclusion is completely enveloped by the host phase (Pride et al., 2004). The EB model has the same form as the equations in Biot theory and has been studied and applied (Huang et al., 2022; Liu et al., 2016, 2018). The operations in the local flow equation of the two models may result in complex numbers, which may affect the mathematical stability of the equations (Liu & Yong, 2016; Xiong et al., 2021b).

Ba et al. (2011) presented the Biot-Rayleigh (BR) theory of poroelasticity to describe seismic wave propagation in media with double porosity. The equation characterizing the local fluid flow (LFF) was established based on the Rayleigh theory. In addition, media with triple porosity (Ma & Ba, 2020) and infinituple porosity (Zhang et al., 2021) were proposed to further characterize sandstone reservoirs and predict seismic dispersion and attenuation. Wang & Tang (2021) and Ba, Zhu, et al. (2023) investigated the effects of multiscale cracks in tight sandstones on seismic wave propagation. In other studies, the elastic properties of sandstone were investigated by experimental measurements (e.g., Chapman et al., 2016; Han et al., 2021; Pimienta et al., 2017; Sahoo et al., 2019; Velcin et al., 2020).

In this study, the BR theory is used to build the model framework and then establish the governing equations of local flow with ML. The proposed modeling approach can be extended to parameter inversion. One solution is to derive parameters while fitting the forward model. Guo et al. (2022) and Liu et al. (2023), for example, made use of this approach during the inversion process, but it cannot be guaranteed that the model parameters obtained after training are always correct. However, it would at least be better than giving incorrect values for them.

The paper is organized as follows. Section 2 presents the proposed modeling approach in which new dynamic equations are obtained by sparse identification. In Section 3, examples are used to show that the local flow equation can be learned accurately. The predictions by the simplified dynamic equations are almost the same as the original BR theory. In Section 4, the new equations are applied to experimental and logging data of tight sandstones and a porosity inversion is performed. Section 5 discusses the differences between the new model and the original model and the impact of the training data on the generalizability of the model. Finally, the conclusions are summarized and further possible directions are discussed in the last section.

2. Methodology

This study focuses on an approach inspired by the DP paradigm (Shen et al., 2023). Figure 1 shows the procedure. The function space that ML can search for is very wide due to the universal approximation theorem (e.g., Cybenko, 1989). A purely data-driven ML-based approach requires a large amount of data, the interpretability is poor, and the generalization and robustness of the surrogate model cannot be guaranteed.

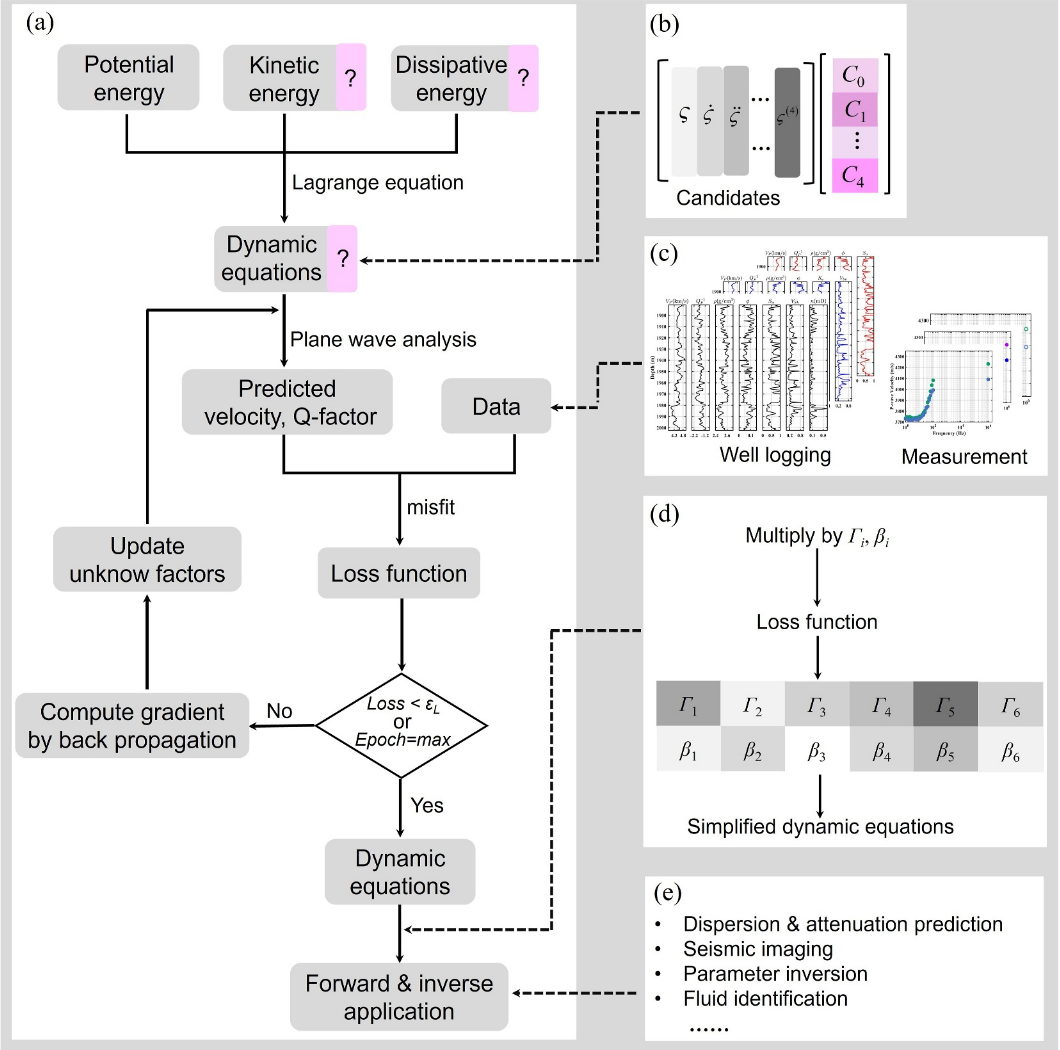

Figure 2. Schematic diagram of the dynamic equations, which includes the basic flowchart of the proposed approach (a), the way for representing the local flow equation (b), data collection (c), the process of sparse learning (d), and the potential applications (e).

In view of this, the proposed ML-based modeling approach attempts to exploit the advantages of both methods. For the specific process, the model is built based on poroelasticity theory, while some relationships or constants, which are usually difficult to determine, are set as unknown factors and then determined by ML (Figure 1). In this way, the modeling workload can be reduced compared with traditional methods.

2.1. The Framework of Dynamic Equations

First, we set up the dynamic equations and then determine the unknown factors with ML. The classical equations include the DPDP, EB and Biot-Rayleigh models (BR), and the unknown factors are elastic constants or the local flow equation describing seismic loss.

As a specific case of the modeling approach shown in Figure 1, BR theory (Ba et al., 2011) is taken as the basis and benchmark, and the governing equation of LFF within the theory is set as unknown factors along with some parameters. The process of setting up the dynamic equations is shown in Figure 2. These equations are derived on the basis of analytical mechanics, just like the BR theory. The potential energy W, kinetic energy T and dissipative energy D of the system can be written as follows:

$$\begin{aligned} W = {} & \frac{1}{2}(A+2N)I_1^2 - 2NI_2 + Q_1 I_1\left(\xi^{(1)} + \phi_2\varsigma\right) + \frac{1}{2}R_1\left(\xi^{(1)} + \phi_2\varsigma\right)^2 \\ & + Q_2 I_1\left(\xi^{(2)} - \phi_1\varsigma\right) + \frac{1}{2}R_2\left(\xi^{(2)} - \phi_1\varsigma\right)^2, \end{aligned} \tag{1}$$

$$T = \frac{1}{2}\rho_{11}\dot{\mathbf{u}}\cdot\dot{\mathbf{u}} + \rho_{12}\dot{\mathbf{u}}\cdot\dot{\mathbf{U}}^{(1)} + \rho_{13}\dot{\mathbf{u}}\cdot\dot{\mathbf{U}}^{(2)} + \frac{1}{2}\rho_{22}\dot{\mathbf{U}}^{(1)}\cdot\dot{\mathbf{U}}^{(1)} + \frac{1}{2}\rho_{33}\dot{\mathbf{U}}^{(2)}\cdot\dot{\mathbf{U}}^{(2)} + T_{\mathrm{LF}}, \tag{2}$$

$$D = \frac{1}{2}b_1\left(\mathbf{u} - \mathbf{U}^{(1)}\right)\left(\mathbf{u} - \mathbf{U}^{(1)}\right) + \frac{1}{2}b_2\left(\mathbf{u} - \mathbf{U}^{(2)}\right)\left(\mathbf{u} - \mathbf{U}^{(2)}\right) + D_{\mathrm{LF}}, \tag{3}$$

where $\mathbf{u}$, $\mathbf{U}^{(1)}$, and $\mathbf{U}^{(2)}$ are the displacements of the solid phase, and fluid in the host and inclusion phases, respectively. ε, $\xi^{(1)}$, and $\xi^{(2)}$ are the divergence of the three displacements, I_1 and I_2 are the first and second strain invariants, ϕ_1 and ϕ_2 are the porosities of the host and inclusion phase, respectively, ς is the increment of the fluid strain in the process of local flow, and T_{LF} and D_{LF} characterize the effect of LFF. In addition, the equations contain six elastic constants A, N, Q_1, Q_2, R_1, R_2, five density coefficients ρ_{11}, ρ_{12}, ρ_{13}, ρ_{22}, ρ_{33}, and two dissipation coefficients b_1 and b_2. An overdot denotes a time derivative. More details about the BR theory can be found in Appendix A or in Ba et al. (2011).

As can be seen in Equation 1, the potential energy W corresponds to the BR theory, while the terms T_{LF} and D_{LF} in the expressions of T and D are considered as unknown factors. It can be assumed that they are functions of ς and the associated quantities in analogy to the BR theory. Substituting Equations 1–3 into Lagrange's equation, we obtain

$$\begin{aligned} & N\nabla^2\mathbf{u} + (A+N)\nabla\varepsilon + Q_1\nabla\left(\xi^{(1)} + \phi_2\varsigma\right) + Q_2\nabla\left(\xi^{(2)} - \phi_1\varsigma\right) = \\ & \rho_{11}\ddot{\mathbf{u}} + \rho_{12}\ddot{\mathbf{U}}^{(1)} + \rho_{13}\ddot{\mathbf{U}}^{(2)} + b_1\left(\dot{\mathbf{u}} - \dot{\mathbf{U}}^{(1)}\right) + b_2\left(\dot{\mathbf{u}} - \dot{\mathbf{U}}^{(2)}\right), \end{aligned} \tag{4a}$$

$$Q_1\nabla\varepsilon + R_1\nabla\left(\xi^{(1)} + \phi_2\varsigma\right) = \rho_{12}\ddot{\mathbf{u}} + \rho_{22}\ddot{\mathbf{U}}^{(1)} - b_1\left(\dot{\mathbf{u}} - \dot{\mathbf{U}}^{(1)}\right), \tag{4b}$$

$$Q_2\nabla\varepsilon + R_2\nabla\left(\xi^{(2)} - \phi_1\varsigma\right) = \rho_{13}\ddot{\mathbf{u}} + \rho_{33}\ddot{\mathbf{U}}^{(2)} - b_2\left(\dot{\mathbf{u}} - \dot{\mathbf{U}}^{(2)}\right), \tag{4c}$$

$$\phi_2\left[Q_1\varepsilon + R_1\left(\xi^{(1)} + \phi_2\varsigma\right)\right] - \phi_1\left[Q_2\varepsilon + R_2\left(\xi^{(2)} - \phi_1\varsigma\right)\right] = F\left(\varsigma, \dot{\varsigma}, \ddot{\varsigma}, \cdots\right), \tag{4d}$$

where the right-hand side of Equation 4d, denoted by F, is unknown because T_{LF} and D_{LF} have not yet been determined. Equation 4 is considered relatively general since it includes the effect of LFF without assuming the inclusion phase to be spherical, as in the BR theory.

The next step is the determination of F. For the traditional modeling approach, which is based on rock physics knowledge, it is necessary to make certain assumptions about the inclusion phase to obtain an analytical relationship. In practice, F can be complex (in the frequency domain) and nonlinear with respect to ς. Seismic propagation and attenuation is usually studied by using a plane-wave analysis method (Carcione, 2022), which, however, can only handle linear equations. Therefore, in this study, F is assumed to be a linear combination of ς and its derivatives with respect to time of various orders. Instead of quantitatively analyzing the mechanism of local flow, similar to the algorithm of SINDy (Brunton et al., 2016), a library of elements that can occur in F is created, and the derivative of ς with respect to time is kept up to the nth order in this study, that is,

$$F\left(\varsigma, \dot{\varsigma}, \ddot{\varsigma}, \cdots\right) = C_0\varsigma + C_1\dot{\varsigma} + C_2\ddot{\varsigma} + C_3\dddot{\varsigma} + \cdots + C_n\varsigma^{(n)}, \tag{5}$$

where the coefficients C_i ($i = 0, 1, \ldots, n$) are regarded as trainable parameters, and n is a hyperparameter. As shown, Equation 5 contains $n+1$ unknown parameters, which is far fewer than the number of parameters in typical NNs, although the universal approximation theorem ensures that NNs can approximate any continuous function. Currently, there is no theoretical method to determine n in Equation 5. Generally, choosing a large value of n can improve the predictive ability, but this may also require more data to determine C_i ($i = 0, 1, \ldots, n$). Conversely, a smaller n may require less data but may not provide sufficient predictive ability. This study suggests selecting a large n if enough data are available, and a smaller n otherwise. In the following examples, it is shown that using a smaller n can result in better prediction performance for the wave propagation model.

By comparison, the expression of F in the BR theory is

$$F = \frac{1}{3}\frac{\rho_f \phi_1^2 \phi_2 \phi_{20}}{\phi_{10}} R_0^2 \cdot \ddot{\zeta} + \frac{1}{3}\frac{\eta \phi_1^2 \phi_2 \phi_{20}}{\kappa_1} R_0^2 \cdot \dot{\zeta}, \tag{6}$$

where the derivation process and symbol introductions can be found in Appendix A. Based on Equation 5, it is not limited to specific scenarios and can encompass a wider range of cases. Specifically, there is no need to consider the shape of the inclusions, nor are complex derivations required; one can directly use Equation 5 as the local flow equation and calibrate the model parameters (C_i, $i = 0, 1, \ldots, n$) based on the given data. In contrast, traditional modeling methods may not require additional data to determine the model parameters, but selecting some of the model parameters can be problematic. Although some parameters may have empirical default values, it remains uncertain whether these values are suitable for all situations. For example, Pride and Berryman (2003a, 2003b) found that the radius of the inclusion affects the dispersion and attenuation values, but they did not provide a method to determine this parameter for different cases. To ensure the applicability of a model, this study suggests that calibrating unknown parameters or relationships using a small amount of data is more reasonable. As a result, a complete wave propagation model is obtained.

Then the loss function must be defined. The labels utilized in this study are the data of the phase velocity V_P and inverse quality factor Q_P^{-1} (if any) of the P wave. Note that the truth of the expression of F does not exist in real applications, and the way to verify its correctness is to check whether the predicted $\hat{V}_P$ and $\hat{Q}_P^{-1}$ match the data based on the learned F. In this study, the unit of V_P is m/s in all the calculations, whose magnitude is generally several thousand. While Q_P^{-1} is usually presented in log10 scale, its absolute value is generally less than 10. Therefore, the loss function is

$$\text{Loss} = \left\| V_P - \hat{V}_P \right\|_2^2 + \lambda \left\| Q_P^{-1} - \hat{Q}_P^{-1} \right\|_2^2, \tag{7}$$

where λ is a weighting factor to balance the two terms and usually taken as 1,000 by considering the magnitude of them, with $\lambda = 0$ if Q_P^{-1} is unavailable.

In addition, some of the parameters required in the system of equations, such as ν_1, ϕ_{10}, K_{b1} and K_{b2}, are usually difficult to determine, while most of them have a significant impact on the results. Therefore, they can be set as trainable parameters together with C_i ($i = 0, 1, \ldots, n$). From the ML point of view, increasing some trainable parameters does not significantly increase the complexity of the algorithm, while it can help to avoid arbitrarily values.

2.2. Simplified Dynamic Equations

Equations 4a–4d contains four equations, that is, there are more equations than that in Biot's theory. This increases the computational complexity (Guo et al., 2022). In this section, synthetic data of wave propagation and attenuation are generated based on the original BR theory, and then sparse identification is performed to obtain a new simplified model. To do this, an ML-based approach is used to filter out necessary terms. Specifically, a given term in Equations 4a–4d is multiplied by a Boolean parameter Γ_i ($i = 1, 2, \ldots, 6$) whose value is either 0 or 1 to determine whether this term is necessary. According to Equation A10 in Appendix A, the matrices $[a_{ij}]$ and $[d_{ij}]$ ($i, j = 1, 2, 3$) are both symmetric, and therefore some Boolean coefficients are assigned to Equations 4a–4d such that the determinant after performing the plane-wave analysis is

$$\begin{vmatrix} \Gamma_1 \cdot (a_{11}k^2 + d_{11}) & \Gamma_2 \cdot (a_{12}k^2 + d_{12}) & \Gamma_3 \cdot (a_{13}k^2 + d_{13}) \\ \Gamma_2 \cdot (a_{12}k^2 + d_{12}) & \Gamma_4 \cdot (a_{22}k^2 + d_{22}) & \Gamma_5 \cdot (a_{23}k^2 + d_{23}) \\ \Gamma_3 \cdot (a_{13}k^2 + d_{13}) & \Gamma_5 \cdot (a_{23}k^2 + d_{23}) & \Gamma_6 \cdot (a_{33}k^2 + d_{33}) \end{vmatrix} = 0. \tag{8}$$

Table 1
Sandstone Properties (Ba et al., 2011; Pride & Berryman, 2003a)

Parameter	Value	Parameter	Value
ϕ_{10}	0.1	K_f	2.5 GPa
ϕ_{20}	0.3	ρ_f	1,040 kg/m^3
ν_1	0.963	η	1.0×10^{-3} Pa·s
K_s	38 GPa	κ_1	1.0×10^{-14} m^2
μ_s	44 GPa	κ_2	1.0×10^{-12} m^2
ρ_s	2,650 kg/m^3		
c_1	10		
c_2	200		
c_S	10		
R_0	0.01 m		

In practice, we set $\Gamma_i = \mathrm{sigmoid}\,(S_l \cdot \theta_i)$, where $i = 1, 2, \ldots, 6$, $\mathrm{sigmoid}(x) = 1/(1 + e^{-x})$, θ_i is a trainable parameter, and S_l is positive a slope parameter, used to approximate values to achieve the approximation to 0 or 1. It is easy to see that sigmoid $(S_l \cdot x)$ becomes steeper as S_l increases. $S_l = 100$ is taken; beyond this value it behaves like the Heaviside function. The element in the third row and third column of the determinant is set to 1 when Γ_3, Γ_5, and Γ_6 are all 0 to avoid singularities. The elastic constants A, N, Q_1, Q_2, R_1 and R_2 here can be different from the original BR theory, but to speed up the training process and improve convergence, the initial value of these constants is calculated by using Equation A7 and then multiplied by a trainable parameter as correction factor separately as: $\beta_1 A$, $\beta_2 N$, $\beta_3 Q_1$, $\beta_4 Q_2$, $\beta_5 R_1$, and $\beta_6 R_2$, where β_i $(i = 1, 2, \ldots, 6)$ can be any positive value.

If Γ_i $(i = 1, 2, \ldots, 6)$ are all 1, Equations 4a–4d is consistent with the BR theory, but it is computationally costly. Therefore, an essential constraint is the sparsity condition which ensures that the predicted V_P and Q_P^{-1} are consistent with the original BR theory and that Γ_i is 0 as much as possible. The loss function is

$$\mathrm{Loss} = \left\| V_P - \hat{V}_P \right\|_2^2 + \lambda_1 \left\| Q_P^{-1} - \hat{Q}_P^{-1} \right\|_2^2 + \lambda_2 \sum_{i=1}^{6} \Gamma_i^2, \tag{9}$$

where λ_1 and λ_2 are two weighting factors, taken as 1,000 and 100, respectively. L_1-or L_2-norm is generally employed as an alternative solution (Brunton et al., 2016; Chen et al., 2021), and the loss function is optimized based on the LASSO and ridge regression algorithms. Here the L_2-norm is used, and they are set as trainable parameters. After training, $\Gamma_i = 0$ $(i = 1, 2, \ldots, 6)$ means that the corresponding term has little influence on the results and can be removed. In contrast, a term is retained if it equals to 1.

3. Method Verification on Synthetic Data

3.1. Learning the Local Flow Equation

First, we investigate whether the local flow equation can be correctly learned from data. For this purpose, dispersion and attenuation data are generated by using Equations 4a–4d, and only a small amount of data is used to train the parameters. Specifically, 10 samples with frequencies within $[1, 10^8]$ Hz are randomly selected and the corresponding V_P and Q_P^{-1} are calculated based on the original BR theory. The required rock physics parameters are listed in Table 1.

The examples in this study are all implemented under the PyTorch framework. In this case, only C_i $(i = 0, 1, \ldots, n)$ are set as trainable parameters. Currently, there is no theoretical method to determine n in Equation 5. This study determined it through trial and error. Here $n = 4$ is assumed, and C_i $(i = 0, 1, \ldots, 4)$ are updated by optimizing the loss function shown in Equation 7, and all parameters and intermediate quantities are the same as those in the BR theory. The hyperparameters are as follows: the mean square error is chosen as the metric of mismatch, the learning rate is 0.01, the optimizer is Adam, and the number of epochs is 80,000.

After training, the learned coefficients C_i $(i = 0, 1, \ldots, 4)$ are shown in Table 2, where the reference values are the results calculated with the BR theory. It can be seen that the predictions are sufficiently accurate with the exception of C_0. Figure 3 shows the comparison of the dispersion and attenuation curves obtained by using the BR theory and Equations 4a–4d and 5 based on the learned C_i $(i = 0, 1, \ldots, 4)$. There are two peaks in the attenuation curve corresponding to the effects of local and global fluid flow on the seismic waves. The results show that although the learned C_0 value does not match the reference value, the two models provide the same propagation and attenuation curves.

Table 2
Comparison of the Predicted Coefficients With Those (Reference) Calculated by the BR Theory

Coefficient	C_0	C_1	C_2	C_3	C_4
Reference value	0	308.80	3.21×10^{-5}	0	0
Precited value	−346.78	308.98	3.32×10^{-5}	0	0

A non-zero C_0 implies the existence of the term $C_0\varsigma$ in F. Equations 4a–4d shows that the left-hand side of the last equation also contains the term of ς

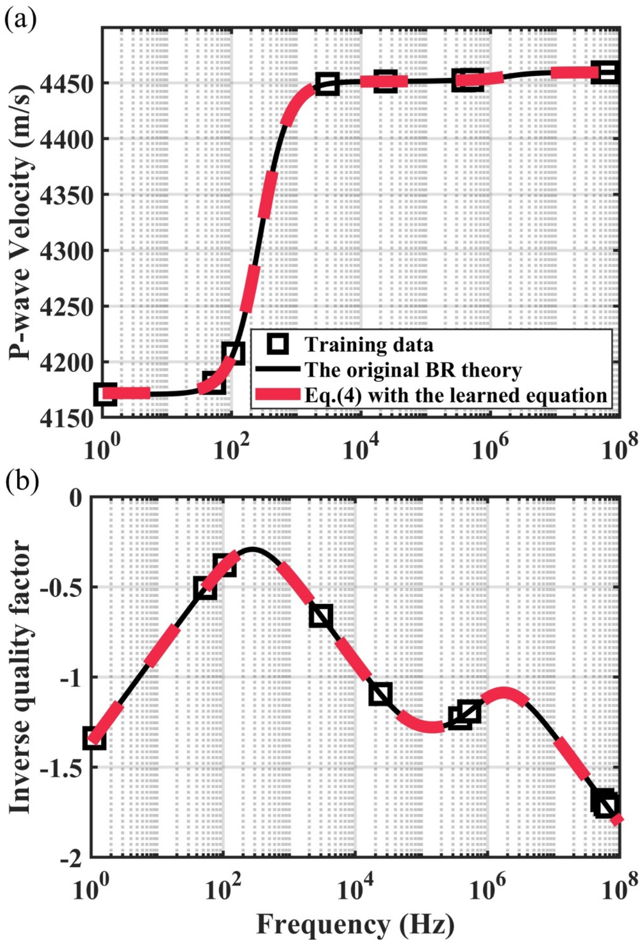

Figure 3. Comparison of the predicted dispersion (a) and attenuation (b) curves by the original BR theory (black solid line) with the established dynamic equations (red dashed line). In this case only C_i $(i = 0, 1, \ldots, n)$ with $n = 4$ are set as trainable parameters.

with the coefficient $U = \phi_2^2 R_1 + \phi_1^2 R_2$, so that the presence of $C_0\varsigma$ can be regarded as a correction. Although the predicted value of C_0 is much smaller than the value of U, it has no significant effect on the results. In other words, the same dispersion and attenuation predictions can be obtained as the original BR theory if the other coefficients are accurate enough. One can neglect the term $C_0\varsigma$ in Equation 5 or do further processing after comparing C_0 with U. Nevertheless, this example shows that the local flow equation can be learned accurately and the dispersion and attenuation predicted by the two models are the same.

In the following, an example for the determination of further trainable parameters is considered, that is, in addition to C_i, the volume ratio ν_1 and the consolidation coefficient c_1 are considered as unknown factors. The hyperparameters are the same as above. The results are listed in Table 3, and Figure 4 shows the comparison of the propagation and attenuation curves of the two models.

Although the predicted C_0 and C_2 are not accurate, the dispersion and attenuation curves of the two models are still almost the same, as C_1, ν_1 and c_1 can be predicted accurately. The reference values show that C_2 is much smaller than C_1, which indicates that the term $C_2\ddot{\varsigma}$ has only a small influence on the results, at least much less than the term $C_1\dot{\varsigma}$. C_0 is still very small compared to U and can be neglected. In fact, some studies (Chen et al., 2021; Rudy et al., 2017) have also found that equations learned from data do not fully match the original models that generate the training data. Perhaps one can assume that the inaccuracy of the secondary factors does not have a significant impact on the results as long as the learning of the primary task is accurate enough. This in turn suggests that some aspects of the original model can be simplified.

3.2. Sparse Identification on the Poroelasticity Theory

In this section, a sparse identification is performed on the BR theory to obtain simplified dynamic equations. To focus on sparsity, the local flow equation is that of the BR theory (see Appendix A). Thus, the trainable parameters are the sparsification coefficients Γ_i $(i = 1, 2, \ldots, 6)$ and six coefficients β_i $(i = 1, 2, \ldots, 6)$ that correct the elastic constants, and their initial values are all 1. Similar to Section 3.1, 10 data points are identified based on the original BR theory, and the properties are the same as those of Table 1. The number of epochs is 100,000, and the other hyperparameters are the same as above.

Figure 5 shows the comparison of the dispersion and attenuation curves determined by using the original BR theory and the simplified dynamic equations. As can be seen, the velocity curves overlap, indicating that the dispersion predicted by the two models is in complete agreement. For the attenuation prediction, the curves overlap in most frequency ranges, but there is a small difference in the middle frequency band due to the removal of some terms in the original equations. Such a result could be acceptable as the overall difference is small and the two predicted peaks corresponding to the global and local flows agree very well. To compare the predictions between the two models under other parameter conditions, see the "Discussion" section below.

Table 3
Comparison of the Predicted Coefficients With Those (Reference) Calculated by the BR Theory

Coefficient	C_0	C_1	C_2	C_3	C_4	ν_1	c_1
Reference value	0	308.80	3.21×10^{-5}	0	0	0.9630	10.00
Precited value	388.54	307.64	5.0×10^{-4}	0	0	0.9634	10.04

Figure 6 shows the variation of Γ_i during the training process. As can be seen, in the training progresses, some coefficients become closer to 0. After training the predicted results are: $\Gamma_1 = 1$, $\Gamma_2 = 1$, $\Gamma_3 = 0$, $\Gamma_4 = 1$, $\Gamma_5 = 0$, $\Gamma_6 = 0$, $\beta_1 = 1.0$, $\beta_2 = 1.0$, $\beta_3 = 0.89$, $\beta_4 = 1.0$, $\beta_5 = 1.0$, $\beta_6 = 1.0$.

The results of β_i indicate that the elastic constants in the simplified equations are the same as the BR theory, except for Q_1 which needs to be corrected by a factor 0.89. The results of Γ_i indicate the BR theory can be simplified as

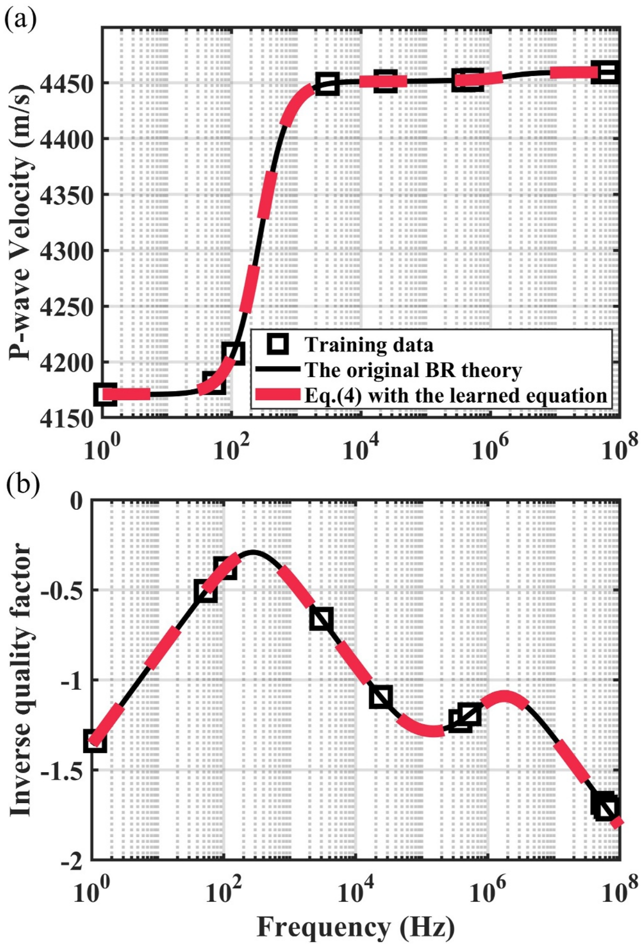

Figure 4. Comparison of the predicted dispersion (a) and attenuation (b) curves by the original BR theory (black solid line) with the established dynamic equations (red dashed line). In this case C_i $(i = 0, 1, \ldots, n)$ with $n = 4$ and ν_1, c_1 are set as trainable parameters.

$$N\nabla^2\mathbf{u} + (A + N)\nabla\varepsilon + Q_1\nabla\xi^{(1)} + \left(\phi_2\beta_3 Q_1 - \phi_1 Q_2\right)\nabla\varsigma$$
$$= \rho_{11}\ddot{\mathbf{u}} + \rho_{12}\ddot{\mathbf{U}}^{(1)} + b_1\left(\dot{\mathbf{u}} - \dot{\mathbf{U}}^{(1)}\right), \tag{10a}$$

$$\beta_3 Q_1\nabla\varepsilon + R_1\nabla\left(\xi^{(1)} + \phi_2\varsigma\right) = \rho_{12}\ddot{\mathbf{u}} + \rho_{22}\ddot{\mathbf{U}}^{(1)} - b_1\left(\dot{\mathbf{u}} - \dot{\mathbf{U}}^{(1)}\right), \tag{10b}$$

$$\left(\phi_2\beta_3 Q_1 - \phi_1 Q_2\right)\varepsilon + \phi_2 R_1\xi^{(1)} = \frac{1}{3}\frac{\rho_f\phi_1^2\phi_2\phi_{20}}{\phi_{10}}R_0^2\ddot{\varsigma}$$
$$+ \frac{1}{3}R_0^2\phi_1^2\phi_2\phi_{20}\frac{\eta}{\kappa_1}\dot{\varsigma} - \left(\phi_2^2 R_1\right.$$
$$\left.- \phi_1^2 R_2\right)\varsigma. \tag{10c}$$

The simplified equations are obtained by omitting Equation 4c, that is, the equation related to $\mathbf{U}^{(2)}$, and changing some terms and coefficients while retaining all constants. It is similar to the dynamic equations describing wave propagation in a single-porosity media. As mentioned above, the EB model has the same form as the Biot equations, but it considers a special case of double porosity media, and the elastic constants involved are related to the constants of two pore types (Pride et al., 2004). In addition, the local flow equation must be retained to describe the seismic wave attenuation mechanism.

Then, by combining with the process of learning the local flow equation from data and ML, C_0, C_3 and C_4 are 0 while C_1 and C_2 are kept as trainable parameters since the term $C_1\dot{\varsigma} + C_2\ddot{\varsigma}$ appears in the BR theory. The simplified equations can be written as

$$\tilde{N}\nabla^2\mathbf{u} + \left(\tilde{A} + \tilde{N}\right)\nabla\varepsilon + \tilde{Q}_1\nabla\xi + \left(\phi_2\tilde{Q}_1 - \phi_1\tilde{Q}_2\right)\nabla\varsigma$$
$$= \rho_{11}\ddot{\mathbf{u}} + \rho_{12}\ddot{\mathbf{U}} + b\left(\dot{\mathbf{u}} - \dot{\mathbf{U}}\right), \tag{11a}$$

$$\tilde{Q}_1\nabla\varepsilon + \tilde{R}_1\nabla\left(\xi + \phi_2\varsigma\right) = \rho_{12}\ddot{\mathbf{u}} + \rho_{22}\ddot{\mathbf{U}} - b\left(\dot{\mathbf{u}} - \dot{\mathbf{U}}\right), \tag{11b}$$

$$\left(\phi_2\tilde{Q}_1 - \phi_1\tilde{Q}_2\right)\varepsilon + \phi_2\tilde{R}_1\xi + \left(\phi_2^2\tilde{R}_1 - \phi_1^2\tilde{R}_2\right)\varsigma = C_1\dot{\varsigma} + C_2\ddot{\varsigma}, \tag{11c}$$

where the indices for the two pore types are removed and the tilde above each symbol means that each of them is first calculated by using Equation A7 and then multiplied by a trainable parameter. Although this example shows that only Q_1 needs to be corrected, β_i are retained in a more general sense in the following examples, and it is found that correcting the six elastic constants can significantly improve the ability of the model to fit the data.

The less costly Equations 11a–11c will serve as the wave propagation model subsequently, which contains eight trainable parameters if all the other required parameters are given.

4. Examples With Real Data

In this section, experimental and logging data are used to verify the effectiveness of the wave propagation model created. Since Equations 11a–11c contain unknown factors and in some cases not all the parameters required for the calculation can be provided, they must first be determined. In other words, the model must be calibrated before further application to ensure that each parameter is reasonably determined or predicted by ML.

4.1. Verification on Experimental Data

Here, the properties of two samples of tight sandstones, numbered TS4 and TS5, are selected for the prediction of wave velocity V_P based on Equations 11a–11c. The two samples are taken from the Jurassic Shaximiao Formation of the Sichuan Basin in China. According to the thin sections, the rock exhibits strong heterogeneity. The

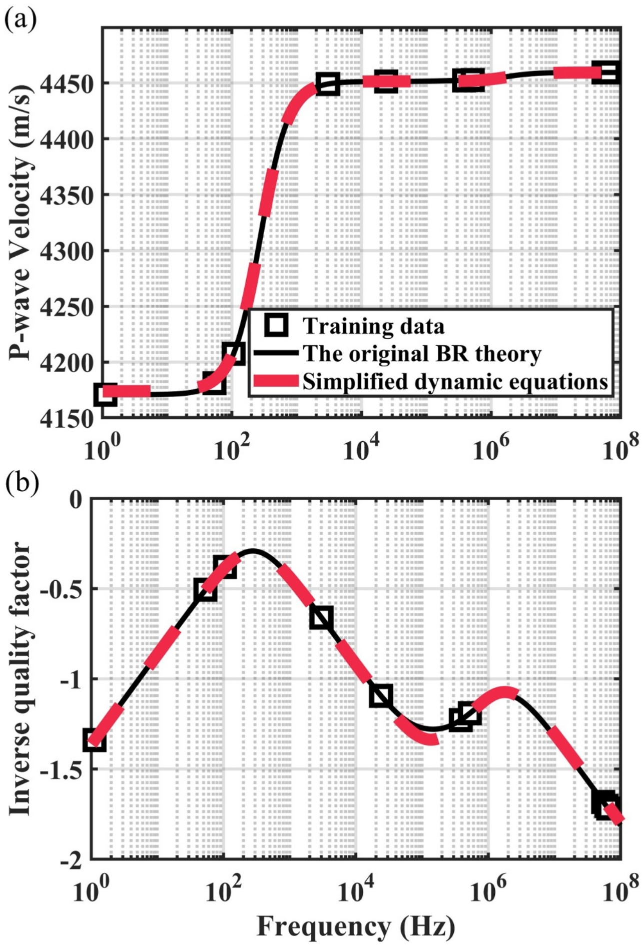

Figure 5. Comparison of the predicted dispersion (a) and attenuation (b) curves by the original BR theory (black solid line) with the simplified dynamic equations (red dashed line).

experimental data of V_P are determined based on the measured Young's modulus, Poisson's ratio and density. The measured V_P corresponding to different frequencies (21 data points at 1–100 Hz and one data point at 1 MHz) are obtained by the oscillation loading of the device, and the measurements of the rock sample saturated with water are selected here. More details on the experimental measurements can be found in Ba, Zhu, et al. (2023), and for the device and data processing, one can refer to Sun et al. (2022). The properties of the two samples are listed in Table 4.

Based on the provided information, ν_1 can be computed as $\nu_1 = (\phi_{20}-\phi)/(\phi_{20}-\phi_{10})$, and K_{b2} can be computed once K_{b1} is given. Therefore, the consolidation coefficient c_1 with the unknown factors β_i ($i = 1, 2, \ldots, 6$) and C_1 and C_2 required by Equations 11a–11c are considered as trainable parameters. Then, only 5 out of the 22 experimental values are taken as the training set to determine them. The loss function is shown in Equation 7 and $\lambda = 0$ since Q_P^{-1} is unavailable. The number of epochs is 10,000, and any other hyperparameters are the same as above. Due to uneven frequency distribution in the measured data, that is, only one data point at the ultrasound band and all other frequencies are within 100 Hz, three scenarios for selecting the five data points are considered, namely sampling from [1, 10], [1, 100], and [1, 10^6] Hz, to investigate the impact of the training data selection on the results.

After training, the predicted dispersion curves are shown in Figure 7 in comparison to the measured velocities. As can be seen, for training data of [1, 10] Hz, the established equations can accurately predict V_P within [1, 100] Hz, indicating a good extrapolation capability. Since the ultrasound frequency far exceeds the coverage range of the training set, the predicted V_P at 1 MHz deviates from the measured value. Nevertheless, thanks to the BR theory, a strong dispersion can be achieved by Equations 11a–11c, which is advantageous for model extrapolation. Extending the sampling range to [1,100] Hz improves the results (Figures 7b and 7e). It is interesting to note that the predicted V_P at 1 MHz is close to the measured value, although the maximum frequency of the training data is 100 Hz. When the training data covers the whole frequency range, the dispersion curve agrees very well with all measured values (Figures 7c and 7f).

This example shows that the unknown factors can be determined on the basis of a small number of data points and then an accurate prediction of the wave velocity is possible. In a purely data-driven approach, all quantitative relationships are unknown and must be learned from the data. In contrast, in the proposed approach, only the unknown factors need to be determined as the framework is built by using the effective poroelasticity theory, which significantly reduces the data set requirements. Nonetheless, the number of model parameters (eight in this example) exceeds the number of data points (five), which constitutes overparameterization. In ML, overparameterized NNs can still exhibit good generalization ability, which classical statistical learning theories cannot explain (Yu et al., 2025). For relevant research, see, for example, Bornschein et al. (2020) and Teresa et al. (2022). Techniques such as L_1/L_2 regularization and early stopping can also be integrated into the proposed approach to reduce the risk of overfitting and ensure the generalization accuracy and stability of the training process.

It is found that correcting the elastic constants with β_i ($i = 1, 2, \ldots, 6$) is important for improving the model's ability to match the data. This indicates that it may not be necessary to use many parameters in Equation 5, in other words, n can be small number when correcting the elastic constants. In addition, in applying this approach in practice, attention should be paid to the coverage of the data points.

Next, the proposed approach is tested by using another data set from experiments on a drill core of the Xujiahe Formation from the northeastern Sichuan Basin, China (Xu et al., 2008; Yin et al., 2017). In the experiment, the wave velocities of brine-saturated rock sample are measured under the nine pressure conditions, namely 2, 5, 7,

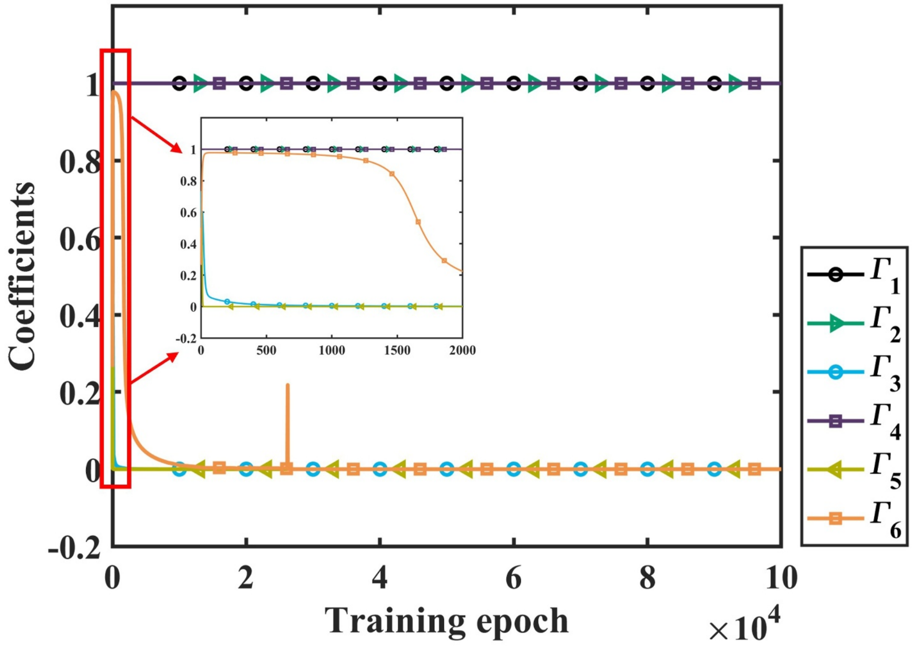

Figure 6. Variation of each sparsity coefficient during the training process and the first 2,000 epochs.

10, 15, 20, 25, 30 and 35 MPa (Yin et al., 2017). For each pressure condition, the wave velocities corresponding to 22 frequencies are measured, with the frequencies of 21 data points in [1, 200] Hz and one data point at 1 MHz. The total porosity ϕ and the porosity of the stiff pores (which serves as the porosity of the host phase ϕ_{10}) at different pressures are given. $\phi(\phi_{10})$ corresponding to the nine pressures are 0.08925(0.08908), 0.08916 (0.08902), 0.08911(0.08900), 0.08903(0.08895), 0.08892(0.08888), 0.08883(0.08880), 0.08874(0.08872), 0.08865(0.08864), and 0.08857(0.08856). Further properties are listed in Table 5.

As can be seen the volume ratio ν_1, and the dry-rock bulk and shear moduli are not provided here, so in addition to C_1, C_2 and β_i $(i = 1, 2, \ldots, 6)$, ν_1, and the three coefficients of consolidation, c_1, c_2, c_S are considered as unknown factors. K_{b1}, K_{b2} and μ_b are obtained from Equation A7.

Table 4
Properties of the Tight Sandstone Samples TS4 and TS5 (Ba, Zhu, et al., 2023)

TS4	Value	TS5	Value
ϕ	0.0877	ϕ	0.1178
ϕ_{10}	0.0826	ϕ_{10}	0.113
ϕ_{20}	0.32	ϕ_{20}	0.32
K_s	32.6 GPa	K_s	32.06 GPa
μ_s	29.8 GPa	μ_s	31.4 GPa
K_b	7.6 GPa	K_b	19.2 GPa
μ_b	11.5 GPa	μ_b	9.5 GPa
ρ_s	2,440 kg/m^3	ρ_s	2,350 kg/m^3
κ	0.149×10^{-15} m^2	κ	0.3985×10^{-15} m^2
K_f	2.25 GPa	K_f	2.25 GPa
ρ_f	1,000 kg/m^3	ρ_f	1,000 kg/m^3
η	1.0×10^{-3} Pa·s	η	1.0×10^{-3} Pa·s

Similar to the previous example, five data points are used as the training set, and three scenarios are considered for the selection of the five points. The hyperparameters are the same as above. After training, the results are shown in Figure 8. The variation of V_P with frequency under different pressures is smaller than that of the samples of TS4 and TS5 as shown in the previous example. From Figure 8a, it can be seen that the prediction by Equations 11a–11c can well fit the data in the low-frequency range, but neither equation can accurately predict V_P at the ultrasonic frequency. The predicted V_P also varies weakly with frequency because the unknown factors are learned from data with limited information. When the detection range of the training data is increased to [1, 100] Hz, the prediction efficiency improves, but there is still some difference at the ultrasonic frequency (Figure 8b). The dispersion curve agrees well with the measured values when the training data covers the whole frequency range (Figure 8c).

This example further shows that the validity of the simplified equations is not a problem here, that is, the change in V_P with frequency can be predicted based on Equations 11a–11c, but relatively poor results will be obtained if the training data used to calibrate the model is insufficient. Further examples can be found in the "Discussion" section below.

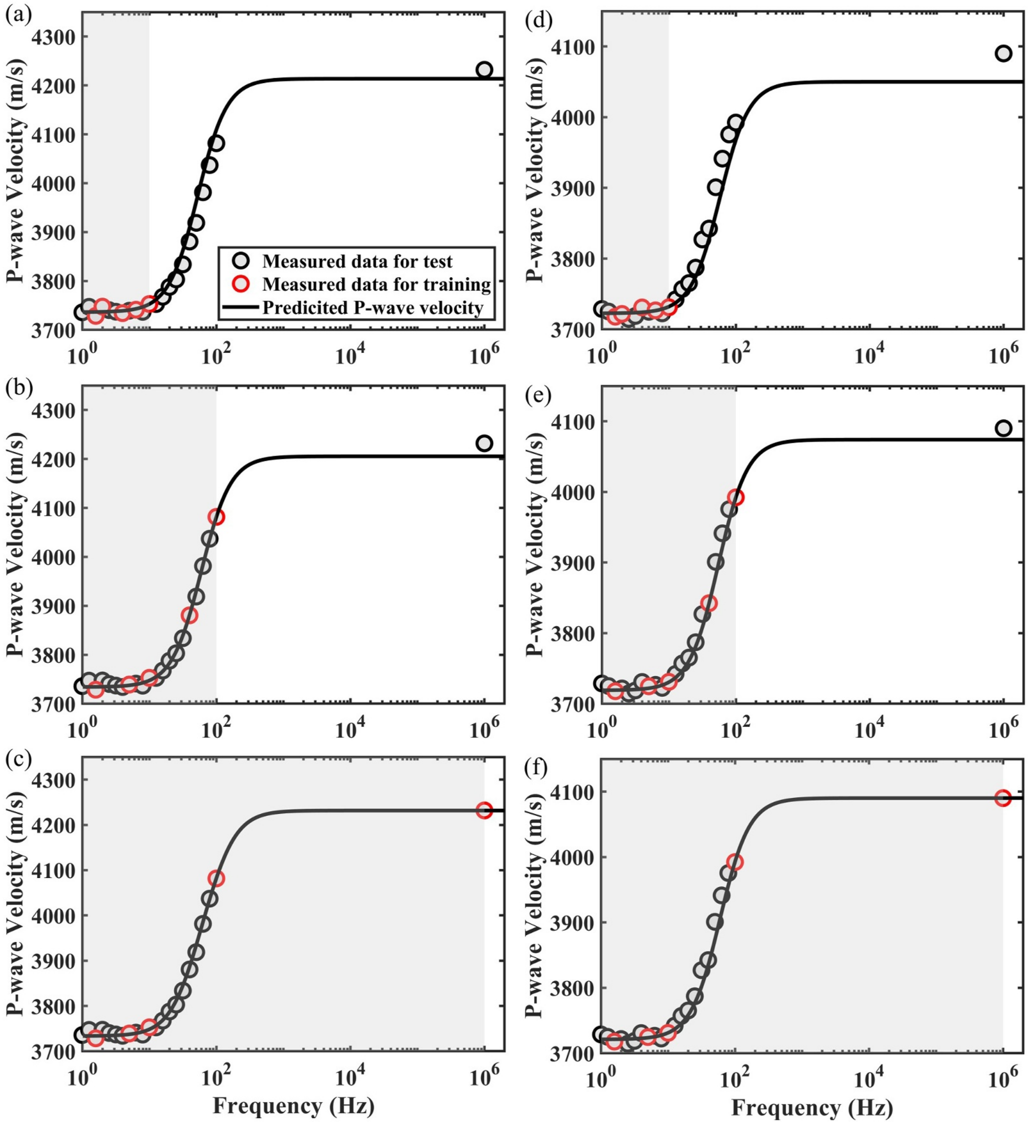

Figure 7. Comparison of the measured velocities and the predicted dispersion curves by the simplified dynamic equations for sample TS4 ((a), (b), (c)) and TS5 ((d), (e), (f)). The gray-shaded region shows the coverage range of the training data.

4.2. Verification on Logging Data

In this section, the effectiveness of the method is verified by using borehole logging data. Unlike experimental data, where most of the rock parameters can be considered fixed, the parameters of physical properties of the reservoir vary with depth in borehole data. Here, logging data were selected from the Chang 7 layer of the

Table 5
Properties of the Tight Sandstone Sample From Xujiahe Formation (Yin et al., 2017)

Property	Value	Property	Value
K_s	40.32 GPa	K_f	2.28 GPa
μ_s	40.69 GPa	ρ_f	1,013 kg/m^3
ρ_s	2,444 kg/m^3	η	1.023×10^{-3} Pa·s
κ	6.3×10^{-17} m^2		

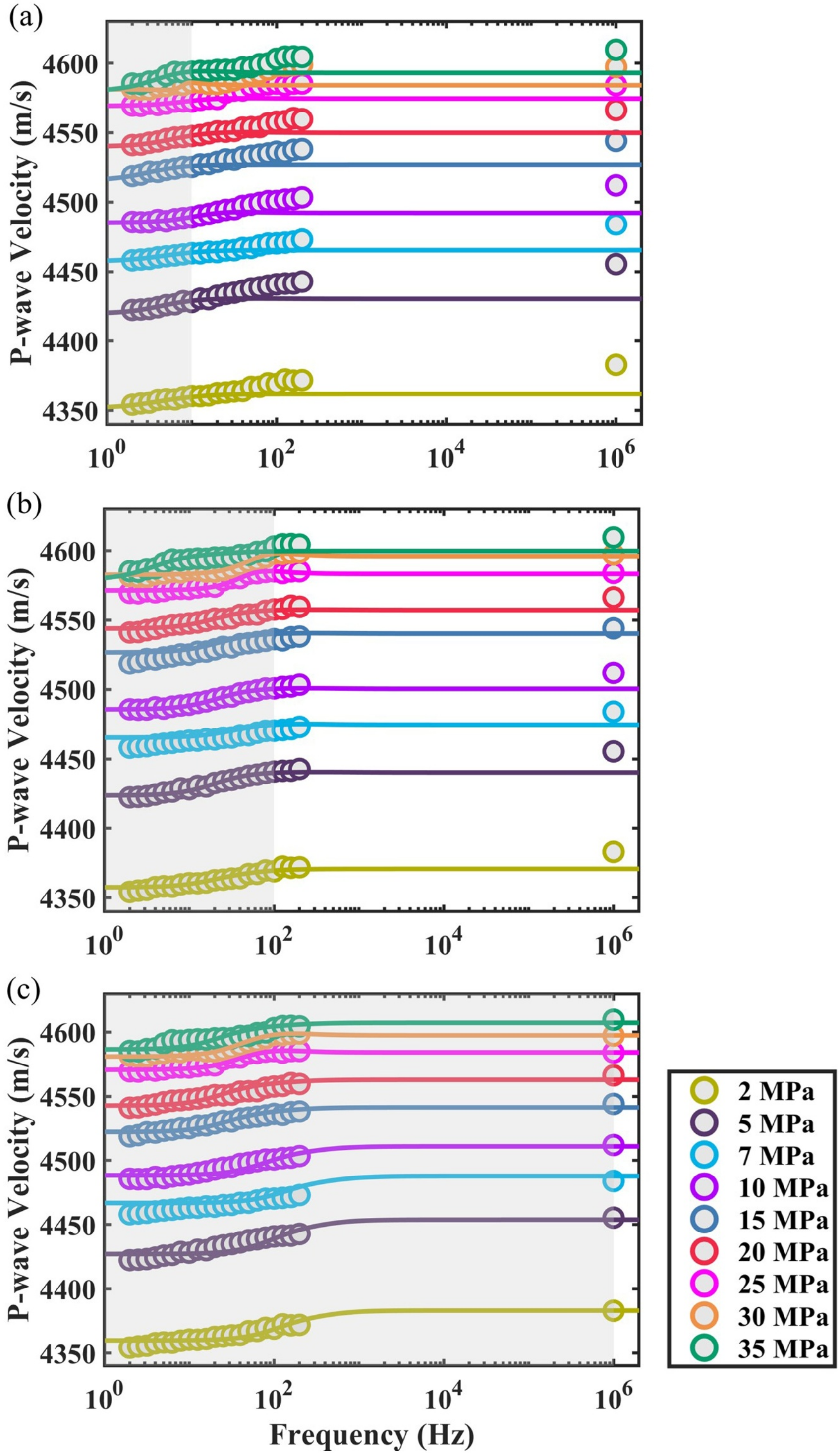

Figure 8. Comparison of the measured velocities (empty circles) and the predicted dispersion curves by the simplified dynamic equations (solid lines). Different colors correspond to different pressures. Subplots (a), (b), and (c) correspond to training data samples from [1, 10], [1, 100], and [1, 10^6] Hz, respectively, and the gray-shaded region marks the coverage range of the training data.

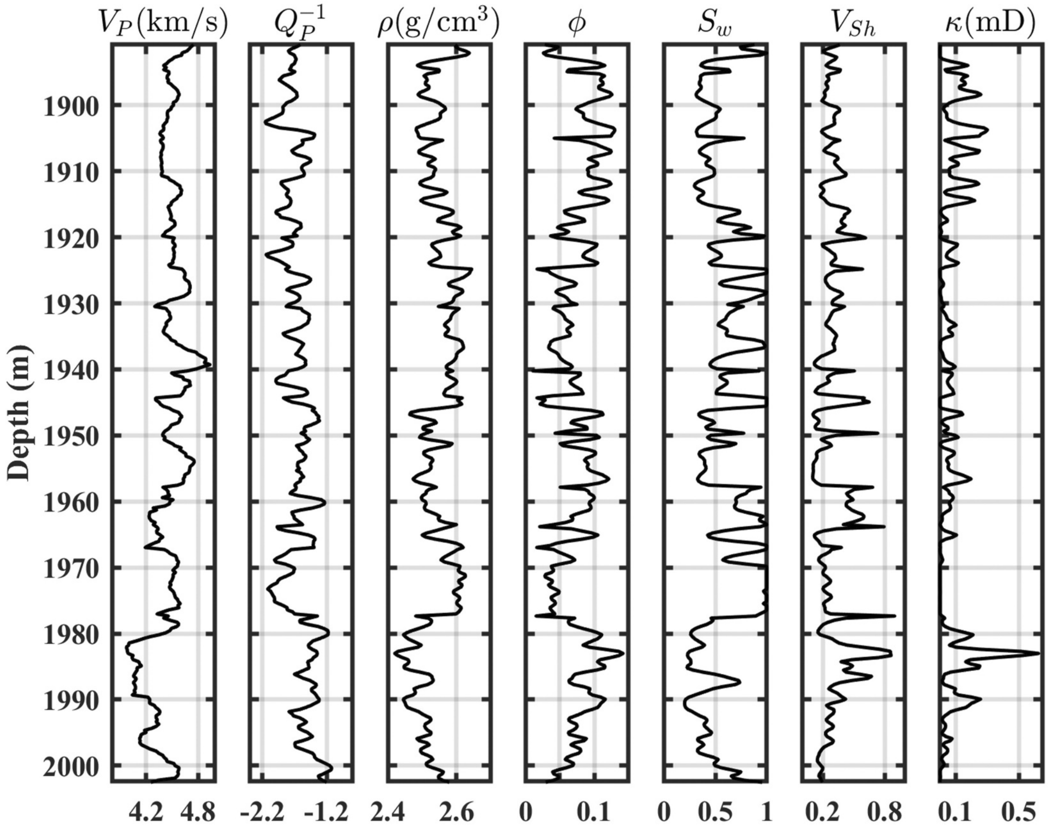

Figure 9. Logging curves from a well of a shale-oil reservoir. The subplots from left to right are P wave velocity, inverse quality factor in log10 scale, density, porosity, water saturation, clay content, and permeability.

Mesozoic Triassic Yanchang Formation in the Ordos Basin, China. The thickness of the Chang 7 layer is about 110 m. It is rich in shale oil deposits. Different types of pore structures can be recognized from the thin sections of the tight rock samples (Ba, Ma, et al., 2023).

Data from 7 boreholes are selected, of which 6 boreholes with a total of 1,278 pairs are referred to as data set A and another borehole with 356 pairs as data set B, as are shown in Figure 9. Each pair of data provides V_P, Q_P^{-1}, ρ, ϕ, S_w, V_{sh} and κ, where V_P is extracted from array sonic logs and Q_P^{-1} is estimated based on an improved frequency shift method (Ba, Ma, et al., 2023; Hu et al., 2013), S_w is water saturation, and V_{sh} is clay content. The reservoir is saturated with oil and water, and the equivalent medium theory (Carcione et al., 2006) is used to calculate the fluid property parameters as

$$K_f = \left(K_{f2} - K_{f1}\right) S_w^2 + K_{f1}, \tag{12a}$$

$$\rho_f = S_w \rho_{f1} + (1 - S_w)\rho_{f2}, \tag{12b}$$

$$\eta = \eta_{f1}\left(\eta_{f2}/\eta_{f1}\right)^{S_w}, \tag{12c}$$

with $K_{f1} = 2.5$ GPa, $K_{f2} = 1.27$ GPa, $\rho_{f1} = 1{,}040$ kg/m^3, $\rho_{f2} = 790$ kg/m^3, $\eta_{f1} = 1.0$ mPa·s, and $\eta_{f2} = 5.0$ mPa·s. In addition, K_s and μ_s are 38 and 44 GPa, respectively, and one can refer to Ba, Ma, et al. (2023) for more details.

It should be noted that there may be different approaches to the determination of unknown factors when applied to logging data. In practical application, in principle, all unspecified parameters should be considered trainable to avoid subjectivity, while too many trainable parameters can also make the training process unstable or difficult to

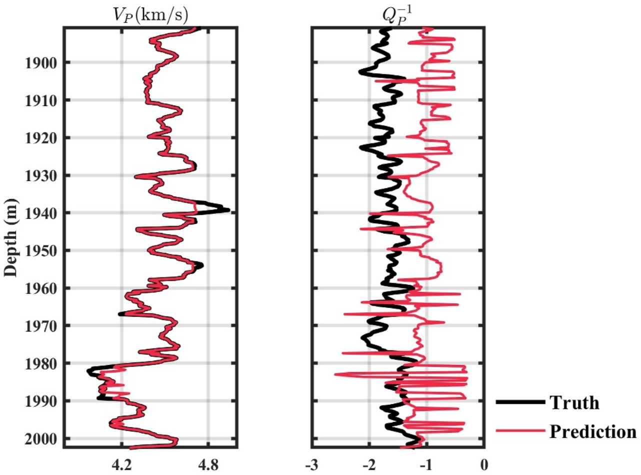

Figure 10. Predicted P-wave velocity and inverse quality factor based on the trained unknown factors, where these for data points at different depths are the same. The black and red solid lines represent the logging data and the predicted values, respectively.

converge. To reduce the number of unknown factors, $c_1 = c_S = 10$ and $c_2 = 200$ are taken, which only has a limited effect on the results, as the elastic constants are still corrected by β_i ($i = 1, 2, \ldots, 6$).

First, the validity of the model created is examined, that is, it is checked whether the predictions by Equations 11a–11c can match the logging data well. Based on the logging data shown in Figure 9, two approaches are considered, namely setting the same unknown factors for data points at different depths (approach I) and varying the unknown factors with depth (approach II). The latter of course corresponds more closely to reality, but involves more parameters that need to be trained. The unknown factors are ν_1, ϕ_{10}, β_i ($i = 1, 2, \ldots, 6$) and C_1 and C_2, and each of them is a single value in approach I, while it is a vector-valued parameter in approach II. The number of epochs in this example is 50,000, the choice of hyperparameters is the same as above, and the loss function is shown in Equation 7.

Figure 10 shows the training results based on approach I, where only V_P and Q_P^{-1} are displayed, as the predicted Q_P^{-1} differs greatly from the true value. Such a result is due to the insufficient predictive power of the model, as the unknown factors are the same at each depth point, which makes it difficult to accurately predict Q_P^{-1} at each point. Nevertheless, the predicted V_P is relatively accurate overall, indicating that if one focuses only on predicting the wave velocity, approach I can be used. After training, predictions such as ν_1 and ϕ_{10} can also be made. However, due to the mismatch of Q_P^{-1}, their accuracy cannot be guaranteed.

Figure 11 shows the training results based on approach II, and as can be seen, the predicted V_P and Q_P^{-1} and the logging values match very well, indicating that the explanatory power of the model performs well and the selected logging data can be explained by the established dynamic equations. This also shows that it is necessary to define unknown factors for parameters at different depth points. In addition, Figure 11 also shows the derived results for

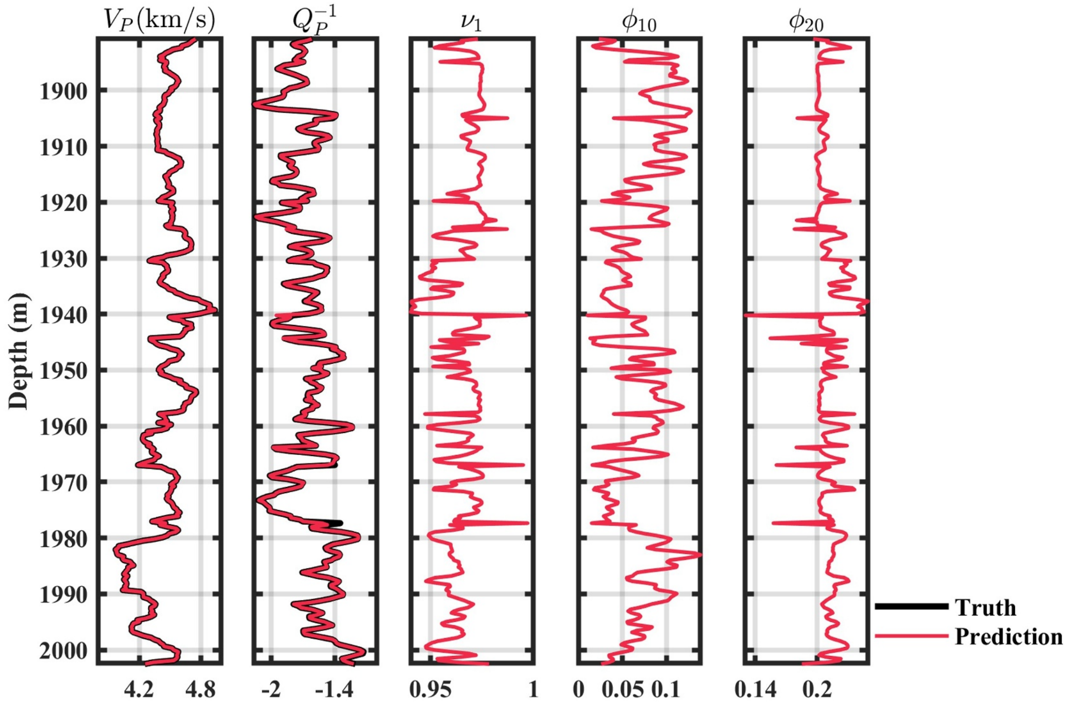

Figure 11. Predicted P-wave velocity and inverse quality factor based on the trained unknown factors, where these vary with depth. The black and red solid lines represent the logging data and the predicted values, respectively.

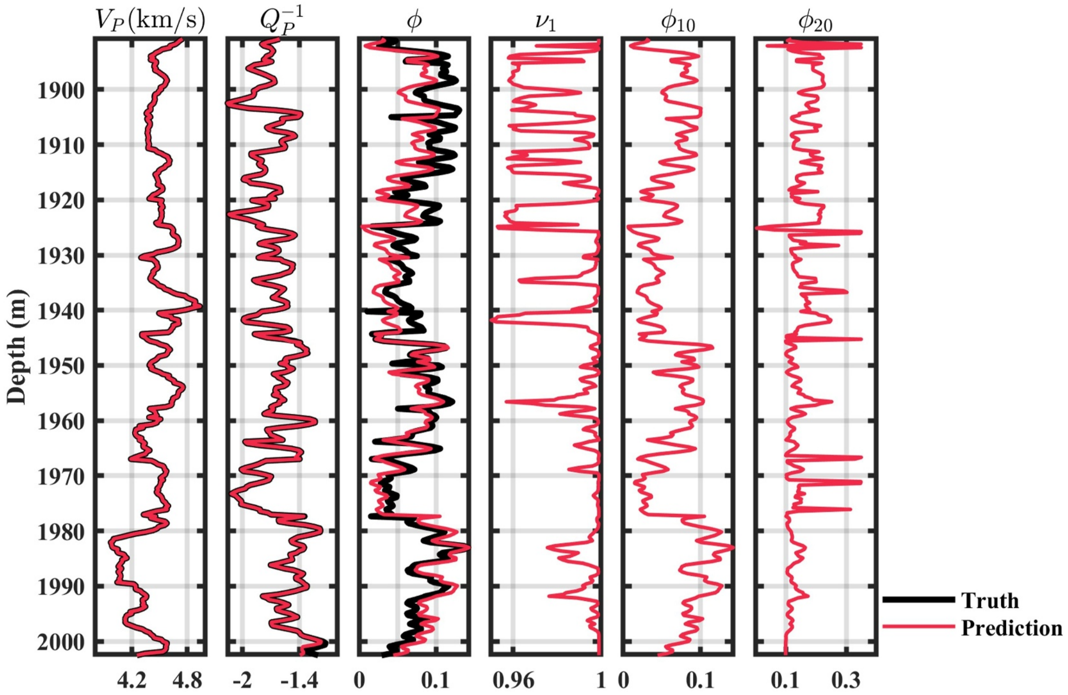

Figure 12. Results of porosity inversion. The black and red solid lines represent the logging data and the predicted values, respectively.

ν_1, ϕ_{10}, and ϕ_{20}. They are not predetermined, but required for the calculation of Equations 11a–11c, so they are determined by training together with the other unknown factors, which can be seen as parameter inversion and is a process of inversion, while the forward model is improved as Equations 11a–11c contain other unknown factors. Despite the lack of true values for comparison, the accuracy of the inversion results can be acceptable as the predicted V_P and Q_P^{-1} and the results based on them match well with the logging data.

In order to check the accuracy of the derived result, a porosity inversion is performed, whereby the data shown in Figure 9 can be used. In particular, the total porosity ϕ in Figure 9 is no longer used in the forward process of Equations 11a–11c and is set as unknown factor together with ν_1, ϕ_{10}, C_1, C_2, and β_i ($i = 1, 2, \ldots, 6$). Note that ρ_s cannot be derived from ρ because ϕ is unknown at this stage and is assumed and fixed as 2,650 kg/m^3. On the other hand, the information of ρ should be used when we creating the loss function since there is a relationship between ρ and ϕ. The loss function is defined as

$$\text{Loss} = \left\| V_P - \hat{V}_P \right\|_2^2 + \lambda_1 \left\| Q_P^{-1} - \hat{Q}_P^{-1} \right\|_2^2 + \lambda_3 \|\rho - \hat{\rho}\|_2^2, \tag{13}$$

where λ_1 and λ_3 are the two weighting factors taken as 1,000 and 10, respectively.

The number of epochs in this example is 50,000 and the selection of the other hyperparameters is the same as above. The result is shown in Figure 12. It can be seen that the predicted V_P and Q_P^{-1} based on Equations 11a–11c agree well with the logging results. The inversion accuracy of ϕ is also good, and the predicted results can match the logging curve in trend, which preliminarily proves the feasibility of parameter inversion based on the proposed approach. The derived values ν_1, ϕ_{10}, and ϕ_{20} are shown in Figure 12, and it is reasonable to believe that their derivative accuracy is also acceptable since the inversion accuracy of ϕ is good.

The effectiveness of porosity inversion in data set A is tested by defining unknown factors for each data point. The comparison between the recording data and the predictions of V_P, Q_P^{-1} and ϕ is shown in Figure 13. From Figures 13a and 13b, it can be seen that the prediction of V_P and Q_P^{-1} based on the unknown factors determined after training agrees well with the logging values, but the accuracy of porosity inversion is not good because many

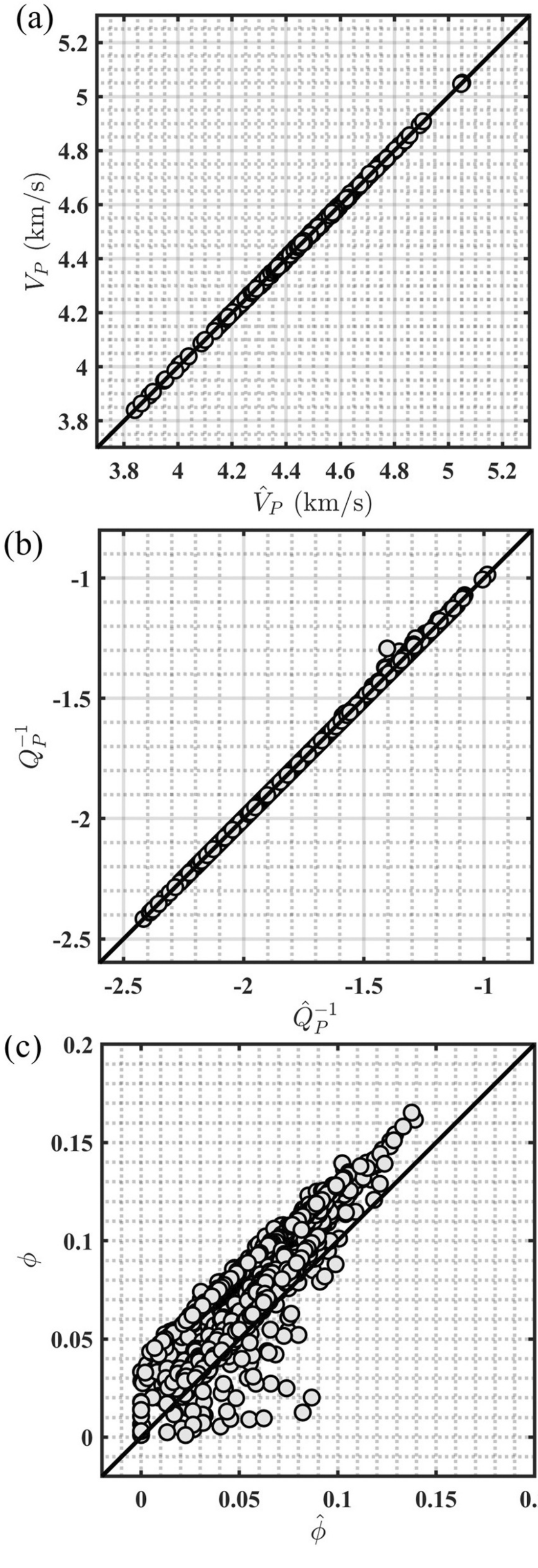

Figure 13. Comparison of the logging data and prediction of P-wave velocity (a), inverse quality factor in log10 scale (b) and the total porosity (c). The black solid line in each plot represents the set of points with equal horizontal and vertical coordinates.

points do not fall on the black line but are concentrated nearby. This phenomenon is subtle as the prediction is not good enough but seems to show a consistent trend. The difference can be very small if the predicted ϕ can be shifted to a fixed value in a certain direction. Figure 12 shows that although the upper half of the predicted ϕ-curve does not match well with the recorded values, a higher accuracy can be achieved if the predicted curve is shifted to the right by a fixed value. This may be due to the non-uniqueness of the solution. To improve this problem, more constraints such as prior information can be added during the training process, but this is beyond the scope of this study.

In addition, as an exception, if no data are available to calibrate the model parameters, we suggest determining the local flow equation and each elastic constant as in the BR theory. Parameter inversion can then still be performed based on the ML framework.

5. Discussion

5.1. Assessment of the Simplified Dynamic Equations

As is shown in Section 3.2, the simplified dynamic equations are obtained by sparse learning. The complexity of the form of Equations 11a–11c lies between the BR theory and the equations of Biot theory. Here, some explanations are given for the construction of the new model based on the results of ML-assisted equation finding. Without being bound to the symbols of the individual elastic coefficients, Equations 11a–11c can be expressed as

$$c_{00}\nabla^2\mathbf{u} + c_{11}\nabla\varepsilon + c_{12}\nabla\xi + c_{13}\nabla\varsigma = \rho_{11}\ddot{\mathbf{u}} + \rho_{12}\ddot{\mathbf{U}} + b\big(\dot{\mathbf{u}} - \dot{\mathbf{U}}\big), \tag{14a}$$

$$c_{21}\nabla\varepsilon + c_{22}\nabla\xi + c_{23}\nabla\varsigma = \rho_{12}\ddot{\mathbf{u}} + \rho_{22}\ddot{\mathbf{U}} - b\big(\dot{\mathbf{u}} - \dot{\mathbf{U}}\big), \tag{14b}$$

$$c_{31}\varepsilon + c_{32}\xi + c_{33}\varsigma = F(\varsigma, \dot{\varsigma}, \cdots) = C_1\dot{\varsigma} + C_2\ddot{\varsigma}. \tag{14c}$$

It is easy to see that Equation 14 are completely changed into the form of the equations of Biot's theory if $\varsigma = 0$ and the third governing equation is removed, i.e. the effect of the LFF is neglected. It is well known that the dispersion and attenuation predicted by the classical Biot theory are often inadequate (e.g., Dvorkin & Nur, 1993; Gurevich & Carcione, 2022), while the BR theory improves the attenuation prediction by introducing ς.

Therefore, Equation 14 can be considered as a modification of Biot theory. In particular, the term $c_{12}\nabla\xi$ in the first governing equation takes into account the effect of fluid deformation on the solid phase. The new model also takes into account the influence of the increase in liquid expansion by adding the term $c_{12}\nabla\varsigma$. Similarly, the term $c_{23}\nabla\varsigma$ is added to the second equation. And the third equation, as a complement, characterizes the relationship between the three strains (ς, ε, and ξ). It should be noted that this is still a wave propagation model for a double-porosity media, while an equivalent treatment applies to the two pore structures, just like the EB model.

In Section 3.2, only one set of rock properties is used to compare the differences between Equations 11a–11c and the BR theory in predicting dispersion and attenuation. To check the differences in multiple sets of parameters, seven parameters ω, ϕ, ϕ_{20}, ν_1, K_s, μ_s, and ρ_s are randomly selected at appropriate intervals as is shown in Table 6, where K_b and μ_b are calculated based on Equation A7, permeability is determined by the Kozeny-Carman

Table 6
Sampling Ranges of Properties for Generating the Data Set

Property	Sampling interval	Property	Sampling interval
ω	$[10^0, 10^8]$ Hz	K_s	[20, 60] GPa
ϕ	[0.01, 0.3]	μ_s	[8, 50] GPa
ϕ_{20}	[0.1, 0.4]	ρ_s	$[1.5, 3]$ g/cm^3
ν_1	[0.6, 0.999]		

relationship (Carman, 1961) as $\kappa = 10\phi^3/(1-\phi)^2$ and the other required parameters are the same as those in Table 1.

In this way, 1 million parameter samples are selected and the dispersion and attenuation are predicted by the two models. The calculation method for the elastic constants A, N, Q_1, Q_2, R_1, and R_2 and the two coefficients C_1 and C_2 in Equations 11a–11c is the same as the BR theory. Figure 14 shows the statistical results of the

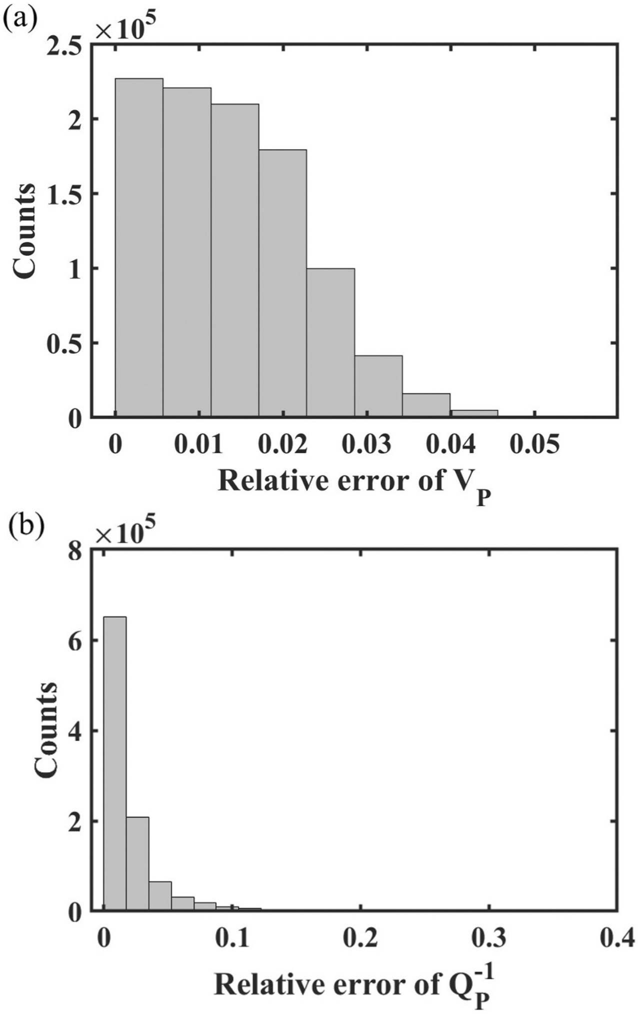

Figure 14. Comparison of dispersion (a) and attenuation (b) predictions between the simplified dynamic equations and the original BR theory.

Table 7
Properties of the Tight Sandstone Sample From the Shahejie Formation (He et al., 2025)

Property	Value	Property	Value
ϕ	0.082	K_f	2.25 GPa
K_s	38 GPa	ρ_f	1,015 kg/m^3
ρ_s	2,640 kg/m^3	η	1.05×10^{-3} Pa·s
κ	5.2×10^{-17} m^2		

relative errors of V_P and Q_P^{-1}, taking V_P as an example and the relative error for each parameter sample is computed by $|(V_{P,\mathrm{new}} - V_{P,\mathrm{BR}})/V_{P,\mathrm{BR}}|$. As can be seen, the velocities predicted by the two models are very close to each other and the relative error is essentially within 5%. Although the difference in predicting Q_P^{-1} is larger, the main error is still within 5%. Therefore, it can be assumed that the simplified equations are not only comparable to the original ones in terms of prediction, but also exhibits a more concise form, which is conducive to practical applications.

5.2. Verification on Other Experimental Data Set

Although the dispersions of the experimental data shown in Figures 7 and 8 are different, a prediction with high accuracy can be achieved by training with less data to determine the unknown factors. However, this does not apply to all experimental data, even if the training data is widely enough.

To further investigate this question, frequency-dependent dispersion data measured experimentally on another tight sandstone sample TS4 (He et al., 2025) from the Shahejie Formation in the Bohai Bay Basin, China, are considered here. In the experiment, the Young's modulus and Poisson's ratio of rock samples saturated with brine under an effective pressure of 5 and 15 MPa, are measured, and the data of V_P corresponding to 16 frequencies are obtained according to the derived bulk and shear moduli of the rock (He et al., 2025). Some rock parameters determined by X-ray diffraction analysis are listed in Table 7. $\mu_s = 40$ GPa is assumed. The unknown factors are ϕ_{10}, ν_1, c_1, c_2, c_S, β_i ($i = 1, 2, \ldots, 6$), C_1, and C_2.

Similarly, five data points are taken as the training set, the hyperparameters are the same as those in Section 4.1, and the results are shown in Figure 15. Similar to Figures 7 and 8, it can be seen that the overall prediction performance improves as the training data coverage increases. When the training data is sampled from [1,100] Hz, the predicted V_P at 1 MHz is much smaller than the measured value, which is worse than the cases in Section 4.1. Moreover, as the training data coverage increases to [1,10^6] Hz, not all data points fall on the dispersion curve (Figure 15c), although they are all concentrated in the vicinity. Further increasing the number of training data to 10 does not significantly improve the effect, which is not shown here. This could be due to the insufficient amount and uneven distribution of the experimental data. Figure 15b shows that the prediction can be good if it is limited to a range of 1,000 Hz and the coverage of the training data is ensured. Alternatively, a better prediction can be achieved by including the squirt flow mechanism in the equations as He et al. (2025).

In the proposed approach, it is necessary to first train unknown factors on the basis of a small amount of data. As is known from the field of ML, factors such as the distribution and amount of training data are crucial for the generalization of surrogate models. By assuming that more experimental data points than training data are used to determine unknown factors, a better prediction can undoubtedly be achieved. However, if the amount of training data is limited, good predictions may only be possible in a limited range. Whereas, it is beyond the scope of this study to identify unknown factors within a limited range of data while enabling the model to make accurate predictions over a larger range.

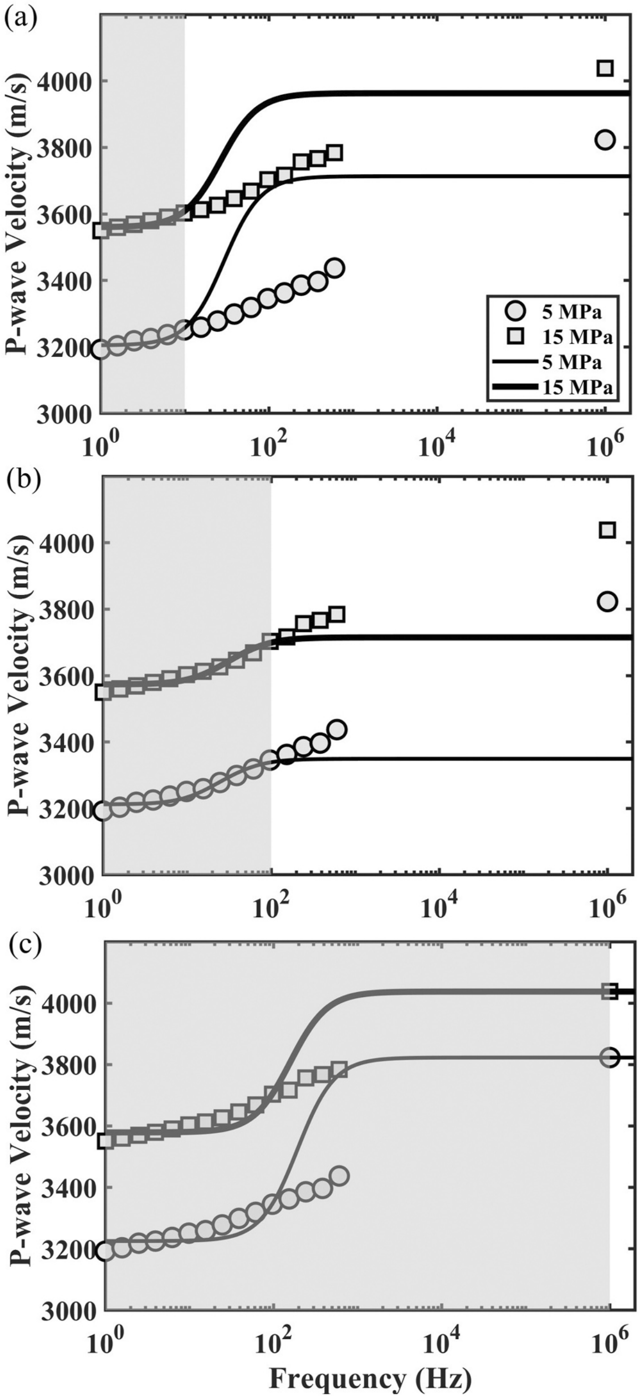

Figure 15. Comparison of the measured velocities and the predicted dispersion curves by the simplified dynamic equations (solid lines) for another sandstone sample. Subplots (a), (b), and (c) correspond to training data samples from [1, 10], [1, 100], and [1, 10^6] Hz, respectively, and the gray-shaded region marks the coverage range of the training data.

6. Conclusions

In this study, a wave propagation approach combining data and ML is proposed. The dynamic equations are established in two steps, that is, wave equations containing unknown factors (media properties) based on the Biot-Rayleigh theory are established, and then data learning is used to describe the anelasticity of LFF in a data-driven manner. After that, a simplified wave equation is obtained by sparse identification. The effectiveness of the approach is validated by using synthetic, experimental and logging data, showing that the simplified equation can accurately predict the P-wave velocity and quality factor. Furthermore, the approach is extended to derive rock parameters while training the unknown factors, achieving a good inversion accuracy. It is still worth investigating which poroelasticity theory can be used to generate an optimal wave equation and which unknown factors are the optimal choice for the different sorts of reservoir rocks and fluid.

Appendix A

This Appendix A provides some details of the Biot-Rayleigh (BR) theory (Ba et al., 2011). A poroelasticity wave propagation model that describes how seismic waves travel through porous media composed of host phase and spherical inclusion phase is developed. In addition to global fluid flow, the influence of LFF on seismic waves has been taken into account. This theory is typically able to quantitatively predict wave dispersion and attenuation in reservoir rocks, making it promising in quantitative seismic interpretation and fluid identification.

Regarding the symbols, ϕ is the total porosity, ϕ_{10} and ϕ_{20} are the absolute porosities of the host and inclusion phases, respectively. ν_1 and ν_2 are the volume ratios of the host and inclusion phase, K_s and K_f are the bulk modulus of the solid matrix and fluid, and μ_s and μ_b denote the shear moduli of the solid matrix and solid skeleton, respectively, K_{b1} and K_{b2} are the bulk moduli of the solid skeletons, c_1, c_2, and c_S are three consolidation coefficients, ρ_s and ρ_f are the densities of the solid and fluid, respectively, η is the viscosity of fluid, κ_1 and κ_2 are the permeabilities of the host and inclusion phases, respectively, and κ is the intrinsic permeability. R_0 denotes the radius of the inclusion phase, and ω is angular frequency. The meanings of the other symbols are given in the main text. There are also the following relationships of $\nu_1+\nu_2 = 1$ and $\phi = \phi_1 + \phi_2$, where $\phi_1 = \nu_1\phi_{10}$ and $\phi_2 = \nu_2\phi_{20}$.

In the BR theory, it is assumed that the inclusions are spherical with radius R_0. In the process of LFF, the interaction is represented by the increment of fluid strain ς. The fluid increment of the inclusion phase is $-\phi_1\varsigma$, with $\phi_1\varsigma \approx 1 - V_0/V = 1 - R_0^3/R^3$ (Ba et al., 2011), where V_0 and V are the static and dynamic volumes of the inclusion, respectively, R is the dynamic radius of the sphere, $\dot{R}$ is the velocity of particles on the spherical surface, $\dot{r}$ is the velocity of particles outside the inclusion, and the continuity condition of fluid on the surface is $4\pi R^2\dot{R}\phi_{20} = 4\pi r^2\dot{r}\phi_{10}$ (Ba et al., 2011). For a single inclusion, the kinetic energy of the LFF process is (Ba et al., 2011; Rayleigh, 1917)

$$T_{\mathrm{LF},1} = \frac{1}{2}\phi_{10}\rho_f\int_R^\infty 4\pi r^2\dot{r}^2\mathrm{d}r = 2\pi\rho_f\frac{\phi_{20}^2}{\phi_{10}}R^3\dot{R}^2, \tag{A1}$$

using the continuity conditions.

Taking the time derivative on both sides of $\phi_1\varsigma \approx 1 - R_0^3/R^3$, gives $\dot{R} \approx \phi_1 R_0\dot{\varsigma}/3$. Then, the total kinetic energy of the LFF process is $T_{\mathrm{LF}} = N_0 T_{\mathrm{LF},1} = 2\pi\rho_f N_0 R^3\dot{R}^2\phi_{20}^2/\phi_{10}$, where N_0 is the number of inclusions per unit volume. According to the relationship $\nu_2 = N_0\cdot 4\pi R^3/3 = \phi_2/\phi_{20}$, $N_0 = 3\phi_2/(4\pi\phi_{20}R^3)$, and we obtain

$$T_{\mathrm{LF}} = \frac{1}{6}\frac{\rho_f\phi_1^2\phi_2\phi_{20}}{\phi_{10}}R_0^2\cdot\dot{\varsigma}^2. \tag{A2}$$

Similar to the derivation of $T_{\mathrm{LF},}$ the dissipation function for a single inclusion is expressed as (Ba et al., 2011)

$$D_{\mathrm{LF},1} = \frac{1}{2}\phi_{10}^2\frac{\eta}{\kappa_1}\int_R^\infty 4\pi r^2\dot{r}^2\mathrm{d}r = 2\pi\phi_{20}^2\frac{\eta}{\kappa_1}R^3\dot{R}^2. \tag{A3}$$

The dissipation function per unit volume can be obtained by dividing $D_{\mathrm{LF},1}$ by V. Then using $\dot{R} \approx \phi_1 R_0\dot{\varsigma}/3$ and $N_0 = 3\phi_2/(4\pi\phi_{20}R^3)$, we obtain

$$D_{\mathrm{LF}} = \frac{3}{2}\frac{\eta\phi_2\phi_{20}}{\kappa_1}\dot{R}^2 = \frac{1}{6}\frac{\eta\phi_1^2\phi_2\phi_{20}}{\kappa_1}R_0^2\dot{\varsigma}^2. \tag{A4}$$

After substituting Equation A2 into Equation 2 and Equation A4 into Equation 3, the potential, kinetic and dissipated energy functions, considering the influence of LFF, are established. Next, by substituting Equations 1–3 into the Lagrange equation

$$\frac{\mathrm{d}}{\mathrm{d}t}\left(\frac{\partial(T-W)}{\partial\dot{\chi}}\right)+\frac{\partial(T-W)}{\partial\chi}+\frac{\partial D}{\partial\dot{\chi}}=0, \tag{A5}$$

where χ is taken as $\mathbf{u}$, $\mathbf{U}^{(1)}$, $\mathbf{U}^{(2)}$ and ς, the final dynamic equations of the BR theory are

$$\begin{aligned} &N\nabla^2\mathbf{u}+(A+N)\nabla\varepsilon+Q_1\nabla\left(\xi^{(1)}+\phi_2\varsigma\right)+Q_2\nabla\left(\xi^{(2)}-\phi_1\varsigma\right)\ = \\ &\rho_{11}\ddot{\mathbf{u}}+\rho_{12}\ddot{\mathbf{U}}^{(1)}+\rho_{13}\ddot{\mathbf{U}}^{(2)}+b_1\left(\dot{\mathbf{u}}-\dot{\mathbf{U}}^{(1)}\right)+b_2\left(\dot{\mathbf{u}}-\dot{\mathbf{U}}^{(2)}\right), \end{aligned} \tag{A6a}$$

$$Q_1\nabla\varepsilon+R_1\nabla\left(\xi^{(1)}+\phi_2\varsigma\right)=\rho_{12}\ddot{\mathbf{u}}+\rho_{22}\ddot{\mathbf{U}}^{(1)}-b_1\left(\dot{\mathbf{u}}-\dot{\mathbf{U}}^{(1)}\right), \tag{A6b}$$

$$Q_2\nabla\varepsilon+R_2\nabla\left(\xi^{(2)}-\phi_1\varsigma\right)=\rho_{13}\ddot{\mathbf{u}}+\rho_{33}\ddot{\mathbf{U}}^{(2)}-b_2\left(\dot{\mathbf{u}}-\dot{\mathbf{U}}^{(2)}\right), \tag{A6c}$$

$$\phi_2\left[Q_1\varepsilon+R_1\left(\xi^{(1)}+\phi_2\varsigma\right)\right]-\phi_1\left[Q_2\varepsilon+R_2\left(\xi^{(2)}-\phi_1\varsigma\right)\right]=\frac{1}{3}\frac{\eta\phi_1^2\phi_2\phi_{20}}{\kappa_1}R_0^2\cdot\dot{\varsigma}+\frac{1}{3}\frac{\rho_f\phi_1^2\phi_2\phi_{20}}{\phi_{10}}R_0^2\cdot\ddot{\varsigma}. \tag{A6d}$$

The expressions of the six elastic constants are

$$\begin{aligned} &A=(1-\phi)K_s-\frac{2}{3}N-\frac{K_s}{K_f}(Q_1+Q_2),\quad N=\mu_b\ =\frac{(1-\phi)\mu_s}{1+c_S\phi}, \\ &Q_1=\frac{\alpha\phi_1K_s}{\alpha+\tau},\quad Q_2=\frac{\phi_2K_s}{1+\tau},\quad R_1=\frac{\phi_1K_f}{\alpha/\tau+1},\quad R_2=\frac{\phi_2K_f}{1/\tau+1}, \\ &\alpha=\frac{\phi_{20}\left[1-(1-\phi_{10})K_s/K_{b1}\right]}{\phi_{10}\left[1-(1-\phi_{20})K_s/K_{b2}\right]},\quad \tau=\frac{K_s(\alpha\phi_1+\phi_2)}{K_f(1-\phi-K_b/K_s)}, \\ &K_b=\left(\frac{\nu_1}{K_{b1}}+\frac{\nu_2}{K_{b2}}\right)^{-1},\quad K_{b1}=\frac{(1-\phi_{10})K_s}{1+c_1\phi_{10}},\quad K_{b2}\ =\frac{(1-\phi_{20})K_s}{1+c_2\phi_{20}}, \end{aligned} \tag{A7}$$

where c_1, c_2 and c_S are the three consolidation constants, and the bulk modulus and shear modulus of rock skeleton are calculated according to the empirical relations provided by Pride & Berryman (2003a, 2003b).

The expressions of the five density constants are

$$\begin{aligned} \rho_{11}\ &=\ (1-\phi_1-\phi_2)\rho_s+0.5(1-\phi_1-\phi_2)\rho_f, \\ \rho_{12}\ &=\ 0.5(\phi_1-\nu_1)\rho_f,\quad \rho_{13}\ =\ 0.5(\phi_2-\nu_2)\rho_f, \\ \rho_{22}\ &=\ 0.5(\phi_1+\nu_1)\rho_f,\quad \rho_{33}\ =\ 0.5(\phi_2+\nu_2)\rho_f. \end{aligned} \tag{A8}$$

The two dissipation coefficients are

$$b_1=\frac{\phi_1\phi_{10}\eta}{\kappa_1},\quad b_2=\frac{\phi_2\phi_{20}\eta}{\kappa_2}. \tag{A9}$$

To avoid symbol confusion, we use j to represent the imaginary unit. Based on a plane-wave analysis, the equations for P waves can be obtained by substituting a plane wave kernel into Equations A6a–A6d, to obtain

$$\begin{vmatrix} a_{11}k^2+d_{11} & a_{12}k^2+d_{12} & a_{13}k^2+d_{13} \\ a_{21}k^2+d_{21} & a_{22}k^2+d_{22} & a_{23}k^2+d_{23} \\ a_{31}k^2+d_{31} & a_{32}k^2+d_{32} & a_{33}k^2+d_{33} \end{vmatrix} = 0, \tag{A10}$$

where

$$\begin{aligned} &a_{11} = A + 2N + \mathrm{j}(\phi_1 Q_2 - \phi_2 Q_1)\, q_1, \quad a_{22} = R_1(1 - \mathrm{j}\phi_2 q_2), \quad a_{33} = R_2(1 + \mathrm{j}\phi_1 q_3), \\ &a_{12} = a_{21} = Q_1 - \mathrm{j}R_1\phi_2 q_1, \quad a_{13} = a_{31} = Q_2 + \mathrm{j}R_2\phi_1 q_1, \quad a_{23} = a_{32} = \mathrm{j}R_2\phi_1 q_2, \\ &q_1 = \mathrm{j}(\phi_2 Q_1 - \phi_1 Q_2)/Z, \quad q_2 = \mathrm{j}\phi_2 R_1/Z, \quad q_3 = -\mathrm{j}\phi_1 R_2/Z, \\ &Z = \frac{1}{3}\omega\phi_1^2\phi_2\phi_{20}R_0^2\left(\frac{\mathrm{j}\eta}{\kappa_1} - \frac{\omega\rho_f}{\phi_{10}}\right) - \left(\phi_2^2 R_1 + \phi_1^2 R_2\right), \end{aligned}$$

and

$$\begin{aligned} &d_{11} = -\rho_{11}\omega^2 + \mathrm{j}\omega(b_1 + b_2), \quad d_{22} = -\rho_{22}\omega^2 + \mathrm{j}\omega b_1, \quad d_{33} = -\rho_{33}\omega^2 + \mathrm{j}\omega b_2, \\ &d_{12} = d_{21} = -\rho_{12}\omega^2 - \mathrm{j}\omega b_1, \quad d_{13} = d_{31} = -\rho_{13}\omega^2 - \mathrm{j}\omega b_2, \quad d_{23} = d_{32} = 0. \end{aligned}$$

Only the fast P wave is used in this study, which corresponds to one root of Equation A10. According to the following definition, one can computed the phase velocity and inverse quality factor (Carcione, 2022) as

$$V_P = \left[\mathrm{Re}\left(\frac{k}{\omega}\right)\right]^{-1}, Q_P^{-1} = \frac{2\,\mathrm{Im}\,(k)}{\mathrm{Re}(k)}, \tag{A11}$$

where k is wave number.

In addition, for the simplified dynamic Equations 11a–11c established in this study, the equation for P waves is (Carcione, 2022)

$$\begin{vmatrix} a'_{11}k^2+d'_{11} & a'_{12}k^2+d'_{12} \\ a'_{21}k^2+d'_{21} & a'_{22}k^2+d'_{22} \end{vmatrix} = 0, \tag{A12}$$

where

$$a'_{11} = A + 2N - \mathrm{j}(\phi_2 Q_1 - \phi_1 Q_2)\, q_1, a'_{12} = a'_{21} = Q_1 - \mathrm{j}R_1\phi_2 q_1, \quad a'_{22} = R_1 - \mathrm{j}\phi_2 q_2,$$

and

$$d'_{11} = -\rho_{11}\omega^2 + \mathrm{j}\omega(b_1 + b_2), \quad d'_{12} = d'_{21} = -\rho_{12}\omega^2 - \mathrm{j}\omega b_1, \quad d'_{22} = -\rho_{22}\omega^2 + \mathrm{j}\omega b_1.$$

Conflict of Interest

The authors declare no conflicts of interest relevant to this study.

Data Availability Statement

The experimental data of tight sandstones shown in Section 4.1 can be found in Ba, Zhu, et al. (2023) and Yin et al. (2017). The logging data shown in Section 4.2 can be found at Xiong et al. (2025). The experimental data of tight sandstones shown in Section 5.2 can be found at He et al. (2025). The open source python package PyTorch is used in this study, and codes in this study are available at Xiong (2025).

Acknowledgments

The work is supported by the National Natural Science Foundation of China (42404128, 42174161) and the Fundamental Research Funds for the Central Universities (B240201131).

References

Ba, J., Carcione, J. M., & Nie, J. X. (2011). Biot-Rayleigh theory of wave propagation in double-porosity media. *Journal of Geophysical Research*, *116*(B6), B06202. https://doi.org/10.1029/2010JB008185

Ba, J., Ma, R., Carcione, J. M., Shi, Y., & Zhang, L. (2023). Effects of pore geometry and saturation on the behavior of multiscale waves in tight sandstone layers [Dataset]. *Journal of Geophysical Research: Solid Earth*, *128*(12), e2023JB027542. https://doi.org/10.1029/2023JB027542

Ba, J., Zhu, H., Zhang, L., & Carcione, J. M. (2023). Effect of multiscale cracks on seismic wave propagation in tight sandstones [Dataset]. *Journal of Geophysical Research: Solid Earth*, *128*(10), e2023JB027474. https://doi.org/10.1029/2023JB027474

Berryman, J. G., & Wang, H. F. (2000). Elastic wave propagation and attenuation in a double-porosity dual-permeability medium. *International Journal of Rock Mechanics and Mining Sciences*, *37*(1–2), 63–78. https://doi.org/10.1016/S1365-1609(99)00092-1

Biot, M. A. (1956). Theory of propagation of elastic waves in a fluid-saturated porous solid. I. Low-frequency range. *Journal of the Acoustical Society of America*, *28*(2), 168–178. https://doi.org/10.1121/1.1908239

Biot, M. A. (1962). Mechanics of deformation and acoustic propagation in porous media. *Journal of Applied Physics*, *33*(4), 1482–1498. https://doi.org/10.1063/1.1728759

Borgomano, J. V., Pimienta, L. X., Fortin, J., & Guéguen, Y. (2019). Seismic dispersion and attenuation in fluid-saturated carbonate rocks: Effect of microstructure and pressure. *Journal of Geophysical Research: Solid Earth*, *124*(12), 12498–12522. https://doi.org/10.1029/2019JB018434

Bornschein, J., Visin, F., & Osindero, S. (2020). Small data, big decisions: Model selection in the small-data regime. In *International conference on machine learning* (pp. 1035–1044). PMLR. https://doi.org/10.5555/3524938.3525035

Brunton, S. L., Proctor, J. L., & Kutz, J. N. (2016). Discovering governing equations from data by sparse identification of nonlinear dynamical systems. *Proceedings of the National Academy of Sciences*, *113*(15), 3932–3937. https://doi.org/10.1073/pnas.1517384113

Carcione, J. M. (2022). *Wave fields in real media. Theory and numerical simulation of wave propagation in anisotropic, anelastic, porous and electromagnetic media* (4th ed.). Elsevier.

Carcione, J. M., Mainardi, F., Qadrouh, A. N., Alajmi, M., & Ba, J. (2024). *Q*: A review. *Surveys in Geophysics*, *45*(5), 1435–1458. https://doi.org/10.1007/s10712-024-09850-y

Carcione, J. M., Picotti, S., Gei, D., & Rossi, G. (2006). Physics and seismic modeling for monitoring CO_2 storage. *Pure and Applied Geophysics*, *163*(1), 175–207. https://doi.org/10.1007/s00024-005-0002-1

Carman, P. C. (1961). *L' écoulement des gaz á Travers les milieux poreux, Bibliothéque des Sciences et Techniques Nucléaires*. Presses Universitaires de France.

Chapman, S., Tisato, N., Quintal, B., & Holliger, K. (2016). Seismic attenuation in partially saturated Berea sandstone submitted to a range of confining pressures. *Journal of Geophysical Research: Solid Earth*, *121*(3), 1664–1676. https://doi.org/10.1002/2015JB012575

Chen, Z., Liu, Y., & Sun, H. (2021). Physics-informed learning of governing equations from scarce data. *Nature Communications*, *12*(1), 6136. https://doi.org/10.1038/s41467-021-26434-1

Cybenko, G. (1989). Approximation by superpositions of a sigmoidal function. *Mathematics of Control, Signals, and Systems*, *2*(4), 303–314. https://doi.org/10.1007/BF02551274

David, E. C., & Zimmerman, R. W. (2012). Pore structure model for elastic wave velocities in fluid-saturated sandstones. *Journal of Geophysical Research*, *117*(B7), B07210. https://doi.org/10.1029/2012JB009195

Dvorkin, J., & Nur, A. (1993). Dynamic poroelasticity: A unified model with the squirt and the Biot mechanisms. *Geophysics*, *58*(4), 524–533. https://doi.org/10.1190/1.1443435

Fang, Z., Ba, J., Guo, Q., & Xiong, F. (2024). Shear-wave velocity prediction of tight reservoirs based on poroelasticity theory: A comparative study of deep neural network and rock physics model. *Geoenergy Science and Engineering*, *240*, 213028. https://doi.org/10.1016/j.geoen.2024.213028

Guo, J., Han, T., Fu, L. Y., Xu, D., & Fang, X. (2019). Effective elastic properties of rocks with transversely isotropic background permeated by aligned penny-shaped cracks. *Journal of Geophysical Research: Solid Earth*, *124*(1), 400–424. https://doi.org/10.1029/2018JB016412

Guo, Q., Ba, J., & Carcione, J. M. (2022). Multi-objective petrophysical seismic inversion based on the double-porosity Biot–Rayleigh model. *Surveys in Geophysics*, *43*(4), 1117–1141. https://doi.org/10.1007/s10712-022-09692-6

Gurevich, B., & Carcione, J. M. (2022). *Attenuation and dispersion of elastic waves in porous rocks: Mechanisms and models*. Society of Exploration Geophysicists.

Han, X., Wang, S., Tang, G., Dong, C., He, Y., Liu, T., et al. (2021). Coupled effects of pressure and frequency on velocities of tight sandstones saturated with fluids: Measurements and rock physics modelling. *Geophysical Journal International*, *226*(2), 1308–1321. https://doi.org/10.1093/gji/ggab157

He, Y., Yuan, S., Tang, G., Sun, C., Feng, Y., Yuan, J., et al. (2025). Experimental observation of moduli dispersion and attenuation at seismic frequencies in saturated tight rock: Effect of microstructure and fluid viscosity [Dataset]. *Geophysical Journal International*, *240*(2), 1308–1330. https://doi.org/10.1093/gji/ggae442

Hu, C., Tu, N., & Lu, W. (2013). Seismic attenuation estimation using an improved frequency shift method. *IEEE Geoscience and Remote Sensing Letters*, *10*(5), 1026–1030. https://doi.org/10.1109/LGRS.2012.2227933

Huang, X., Greenhalgh, S., Han, L., & Liu, X. (2022). Generalized effective Biot theory and seismic wave propagation in anisotropic, poroviscoelastic media. *Journal of Geophysical Research: Solid Earth*, *127*(3), e2021JB023590. https://doi.org/10.1029/2021JB023590

Li, H., Wang, D., Gao, J., Zhang, M., Wang, Y., Zhao, L., & Yang, Z. (2020). Role of saturation on elastic dispersion and attenuation of tight rocks: An experimental study. *Journal of Geophysical Research: Solid Earth*, *125*(4), e2019JB018513. https://doi.org/10.1029/2019JB018513

Li, Y. E., O'Malley, D., Beroza, G., Curtis, A., & Johnson, P. (2023). Machine learning developments and applications in Solid-Earth geosciences: Fad or future? *Journal of Geophysical Research: Solid Earth*, *128*(1), e2022JB026310. https://doi.org/10.1029/2022JB026310

Liu, J., & Yong, W. A. (2016). Stability analysis of the Biot/squirt models for wave propagation in saturated porous media. *Geophysical Journal International*, *204*(1), 535–543. https://doi.org/10.1093/gji/ggv463

Liu, M., Vashisth, D., Grana, D., & Mukerji, T. (2023). Joint inversion of geophysical data for geologic carbon sequestration monitoring: A differentiable physics-informed neural network model. *Journal of Geophysical Research: Solid Earth*, *128*(3), e2022JB025372. https://doi.org/10.1029/2022JB025372

Liu, X., Greenhalgh, S., Zhou, B., & Greenhalgh, M. (2018). Effective Biot theory and its generalization to poroviscoelastic models. *Geophysical Journal International*, *212*(2), 1255–1273. https://doi.org/10.1093/gji/ggx460

Liu, X., Greenhalgh, S., Zhou, B., & Heinson, G. (2016). Generalized poroviscoelastic model based on effective Biot theory and its application to borehole guided wave analysis. *Geophysical Journal International*, *207*(3), 1472–1483. https://doi.org/10.1093/gji/ggw345

Ma, R., & Ba, J. (2020). Coda and intrinsic attenuations from ultrasonic measurements in tight siltstones. *Journal of Geophysical Research: Solid Earth*, *125*(4), e2019JB018825. https://doi.org/10.1029/2019JB018825

Müller, T. M., Gurevich, B., & Lebedev, M. (2010). Seismic wave attenuation and dispersion resulting from wave-induced flow in porous rocks—A review. *Geophysics*, *75*(5), 75A147–75A164. https://doi.org/10.1190/1.3463417

Osorio, N., Sahimi, M., Barati, R., & Ghanbarian, B. (2025). Predicting elastic moduli of heterogeneous porous media by percolation theory and effective-medium approximation. *Journal of Geophysical Research: Solid Earth*, *130*(4), e2024JB030836. https://doi.org/10.1029/2024jb030836

Pimienta, L., Borgomano, J. V. M., Fortin, J., & Guéguen, Y. (2017). Elastic dispersion and attenuation in fully saturated sandstones: Role of mineral content, porosity, and pressures. *Journal of Geophysical Research: Solid Earth*, *122*(12), 9950–9965. https://doi.org/10.1002/2017JB014645

Pride, S. R., & Berryman, J. G. (2003a). Linear dynamics of double-porosity dual-permeability materials. I. Governing equations and acoustic attenuation. *Physical Review E*, *68*(3), 036603. https://doi.org/10.1103/PhysRevE.68.036603

Pride, S. R., & Berryman, J. G. (2003b). Linear dynamics of double-porosity dual-permeability materials. II. Fluid transport equations. *Physical Review E*, *68*(3), 036604. https://doi.org/10.1103/PhysRevE.68.036604

Pride, S. R., Berryman, J. G., & Harris, J. M. (2004). Seismic attenuation due to wave-induced flow. *Journal of Geophysical Research*, *109*(B1), 59–70. https://doi.org/10.1029/2003jb002639

Rayleigh, L. (1917). On the pressure developed in a liquid during the collapse of a spherical cavity. *Philosophical Magazine*, *34*(200), 94–98. https://doi.org/10.1080/14786440808635681

Rudy, S. H., Brunton, S. L., Proctor, J. L., & Kutz, J. N. (2017). Data-driven discovery of partial differential equations. *Science Advances*, *3*(4), e1602614. https://doi.org/10.1126/sciadv.1602614

Sahoo, S. K., North, L. J., Marín-Moreno, H., Minshull, T. A., & Best, A. I. (2019). Laboratory observations of frequency-dependent ultrasonic P-wave velocity and attenuation during methane hydrate formation in Berea sandstone. *Geophysical Journal International*, *219*(1), 713–723. https://doi.org/10.1093/gji/ggz311

Shen, C., Appling, A. P., Gentine, P., Bandai, T., Gupta, H., Tartakovsky, A., et al. (2023). Differentiable modelling to unify machine learning and physical models for geosciences. *Nature Reviews Earth and Environment*, *4*(8), 552–567. https://doi.org/10.1038/s43017-023-00450-9

Smith, T. M., Sayers, C. M., & Sondergeld, C. H. (2009). Rock properties in low-porosity/low-permeability sandstones. *The Leading Edge*, *28*(1), 48–59. https://doi.org/10.1190/1.3064146

Song, W., Jiang, S., Camps-Valls, G., Williams, M., Zhang, L., Reichstein, M., et al. (2024). Towards data-driven discovery of governing equations in geosciences. *Communications Earth and Environment*, *5*(1), 589. https://doi.org/10.1038/s43247-024-01760-6

Sun, C., Fortin, J., Borgomano, J. V., Wang, S., Tang, G., Bultreys, T., & Cnudde, V. (2022). Influence of fluid distribution on seismic dispersion and attenuation in partially saturated limestone. *Journal of Geophysical Research: Solid Earth*, *127*(5), e2021JB023867. https://doi.org/10.1029/2021JB023867

Teresa, N., Hogg, D. W., & Villar, S. (2022). Dimensionality reduction, regularization, and generalization in overparameterized regressions. *SIAM Journal on Mathematics of Data Science*, *4*(1), 126–152. https://doi.org/10.1137/20M1387821

Tsai, W. P., Feng, D., Pan, M., Beck, H., Lawson, K., Yang, Y., et al. (2021). From calibration to parameter learning: Harnessing the scaling effects of big data in geoscientific modeling. *Nature Communications*, *12*(1), 5988. https://doi.org/10.1038/s41467-021-26107-z

Velcin, H., Dautriat, J., Sarout, J., Esteban, L., & Godel, B. (2020). Experimental reactivation of shear-fractured Berea and Boise sandstones by brine or liquid CO2 injection at depth. *Journal of Geophysical Research: Solid Earth*, *125*(2), e2019JB018281. https://doi.org/10.1029/2019JB018281

Viswanathan, H. S., Ajo-Franklin, J., Birkholzer, J. T., Carey, J. W., Guglielmi, Y., Hyman, J. D., et al. (2022). From fluid flow to coupled processes in fractured rock: Recent advances and new frontiers. *Reviews of Geophysics*, *60*(1), e2021RG000744. https://doi.org/10.1029/2021RG000744

Wang, H. M., & Tang, X. M. (2021). Inversion of dry and saturated P-and S-wave velocities for the pore-aspect-ratio spectrum using a cracked porous medium elastic wave theory. *Geophysics*, *86*(6), A57–A62. https://doi.org/10.1190/geo2021-0071.1

Xiong, F. (2025). Machine learning assisted wave propagation model establishing and numerical examples [Code]. *Zenodo*. https://doi.org/10.5281/zenodo.16432268

Xiong, F., Ba, J., & Fang, Z. (2025). Logging data used for verifying parameter inversion [Dataset]. *Zenodo*. https://doi.org/10.5281/zenodo.16431216

Xiong, F., Ba, J., Gei, D., & Carcione, J. M. (2021a). Data-driven design of wave-propagation models for shale-oil reservoirs based on machine learning. *Journal of Geophysical Research: Solid Earth*, *126*(12), e2021JB022665. https://doi.org/10.1029/2021JB022665

Xiong, F., Liu, J., Guo, Z., & Liu, J. (2021b). Stability analysis-based reformulation of wave equations for poro-elastic media saturated with two fluids. *Geophysical Journal International*, *226*(1), 327–344. https://doi.org/10.1093/gji/ggab117

Xiong, F., & Yong, W. A. (2022). Learning stable seismic wave equations for porous media from real data. *Geophysical Journal International*, *230*(1), 349–362. https://doi.org/10.1093/gji/ggac082

Xu, Z., Zhang, X., Wu, S., & Zhao, Y. (2008). Genesis of the low-permeability reservoir bed of Upper Triassic Xujiahe formation in Xinchang gas field, western Sichuan Depression. *Petroleum Science*, *5*(3), 230–237. https://doi.org/10.1007/s12182-008-0035-z

Yin, H., Zhao, J., Tang, G., Zhao, L., Ma, X., & Wang, S. (2017). Pressure and fluid effect on frequency-dependent elastic moduli in fully saturated tight sandstone [Dataset]. *Journal of Geophysical Research: Solid Earth*, *122*(11), 8925–8942. https://doi.org/10.1002/2017JB014244

Yu, L., Miao, Y., Zhu, Y., Gao, X. S., & Zhang, L. (2025). Generalizability of neural networks minimizing empirical risk based on expressive power. In *The thirteenth international conference on learning representations*.

Yu, S., & Ma, J. (2021). Deep learning for geophysics: Current and future trends. *Reviews of Geophysics*, *59*(3), e2021RG000742. https://doi.org/10.1029/2021RG000742

Zhang, L., Ba, J., & Carcione, J. M. (2021). Wave propagation in infinituple-porosity media. *Journal of Geophysical Research: Solid Earth*, *126*(4), e2020JB021266. https://doi.org/10.1029/2020JB021266